UNIVERSITÀ DI PISA

Dottorato di Ricerca in Ingegneria Industriale

*Curriculum in Ingegneria Nucleare e Sicurezza Industriale*

Ciclo XXXI

# Silicon photomultiplier current and prospective applications in biological and radiological photonics


**Author**

Ing. Marialisa Staglianò

**Supervisors**

Prof. Francesco d'Errico

Prof. Alberto Del Guerra

Dott. Luis Abegão

**Coordinator of the PhD Program**

Prof. Giovanni Mengali

March 2019

# Abstract

The detection of low-intensity light is a crucial issue in many aspects of science and technology. So far, the solution has involved extremely delicate and somewhat bulky devices, the photomultiplier tubes (PMT), providing high sensitivity but suffering from fragility and susceptibility to interference. The silicon photomultiplier (SiPM) is a new solid-state photon detector that provides a new solution for a wide range of photometry applications in fields as diverse as medicine, biology, environmental science, chemistry, physics, and nuclear physics.

SiPMs are on a par with conventional PMTs in terms of internal gain and photon detection efficiency, while they are undoubtedly superior in terms of mechanical robustness, compact size, electronic stability, low power consumption, and affordability. SiPMs offer the unquestionable advantages in ionizing radiation measurements based on light emitting sensors, both for industrial nuclear technology applications and for hybrid diagnostic imaging techniques.

In this thesis, two different application fields of SiPMs have been proposed, developed and tested.

The first one is the use of SiPMs in scintillation detectors: in particular a miniaturized beta probe was developed for measurements of tissue differential uptake of a radio-drug beta emitter. The proposed solution is based on the use of a plastic scintillator optically coupled with a SiPM.

The second application is the realization of a luminescence reader for passive dosimeters based also on SiPM for detection and on LED for stimulation.

# Contents

# List of figure

# 1 Introduction

Detecting low intensity light with highly efficient and highly scalable sensors is crucial in many aspects of science and technology. For example, photoluminescent bioprobes triggered by single photon absorption linear optics or by other type of processes, such as chemiluminescence, have an important role as miniaturized biosensors for the biological and biomedical field [1]. Nonlinear optical phenomena [2] also play a role in life sciences, for example when coherent light beams at high optical intensities are used to trigger a faint second harmonic luminescent emission (SHG) from organic compounds in solution [3, 4]. Indeed, two-photon excited fluorescence (TPEF) [5] combined with SHG imaging provides extremely promising bioprobes [6-8], such as those for the identification of early nodules in calcified aortic-valve disease [9]. The detection of light is also fundamental in the field of ionizing radiation detection and measurement [10], where prompt radioluminescence and optically stimulated luminescence are widely used for field characterization and dosimetry [11, 12]. More recently, the detection of light scattered by neutron-induced bubbles inside superheat emulsions has been reported as an efficient detector readout approach [13, 14]. Undoubtedly, any application based on low-intensity light emissions will require photosensors with superior photon detection performance combined with mechanical robustness, and scalable size.

So far, the solution for measuring low-intensity light has involved extremely delicate and somewhat bulky devices, the photomultiplier tubes, providing high sensitivity but suffering from fragility and susceptibility to magnetic interference. The introduction of the silicon photomultiplier (SiPM), also called multi-pixel photon counter, has brought a real revolution in the field of measuring light. The SiPM uses an array of CMOS compatible photodiodes, each operating in Geiger mode (GM) with an integrated quenching circuit, connected in parallel on a silicon wafer. A photon interacting with any photodiode produces a pulse of current at the sensor output, and the sum of all individual current pulses from each photodiode produces the total output from the light recorded in a timeframe. Therefore, the total output current is proportional to the incident photon flux. The total SiPM gain is around one million, that is significantly higher than that of a normal avalanche photodiode (APD), which is typically around one hundred. This recent technology combines the positive features of conventional photomultiplier tubes (PMTs),

i.e., high gain, sensitivity, and stability with those of silicon APDs, i.e. small size, low voltage operation, and ruggedness [15].

In order to fully appreciate the advantages offered by SiPMs, it is useful to review the prior technology of APDs and PMTs. The APD is a silicon solid-state photo-detectors that convers light to a proportional electrical signal using the photoelectric effect. This detector requires a high reverse-bias voltage (~200 V) to create the necessary avalanche effect.

Its physical structure is robust, insensitive to magnetic fields and compact [16]; on the other hand, its response has a strong dependence on temperature and it is not suitable for single photon detection due to its low internal gain [15]. The conventional PMT was the first detector that can convert a weak light signal into a measurable electric one. In PMTs, an input photocathode converts light into electrons that are accelerated against a series of electrodes (dynodes) positioned in cascade, thus extracting more electrons from dynode to dynode due to a high bias voltage (~1000 V). A vacuum tube is necessary for proper operation and magnetic fields will cause interference by deflecting the electrons [10].

The SiPMs' insensitivity to magnetic interferences combined with their compact dimensions are two of the main reasons for their wide utilization. One of the first reported SiPM viability studies was conducted for the Tesla Hadron Tile Calorimeter [17], where SiPMs were coupled with a scintillator and a wavelength shifter (WLS) providing unique energy and time resolution in nuclear particle calorimetry compared with PMTs and with hybrid photo-diodes [18-20]. This study paved the way to applications in many different research fields [21-28].

The SiPMs' compactness, robustness and high photon detection efficiency makes them possibly the best miniaturized optical sensors [29]. Also, SiPMs are highly scalable: depending on the application it is possible to use a matrix of a few tens of cells [30] or up to thousands of cells [31] just adjusting the electronics front-end. Another major advantage of SiPMs is their low bias voltage, an order of magnitude lower than in PMTs [32], allowing the design of compact, affordable and low power-consumption devices [33].

In this work, all the above SiPM characteristics were utilized to realize devices for two different type of applications. The SiPM, coupled with a scintillator, is a solution to build a scintillation detector for future endovascular and intra-myocardial probe in an

integrated theranostic system utilizing molecularly-targeted radiotracers to deliver localized intra-myocardial therapies. Other intraoperative beta probes for radio-guided tumor surgery have been already proposed in literature [34], but the solution here described focuses on a new endovascular application that requires stringent technical specifications such as low voltage, miniaturization and high time-resolution [35]. The feasibility study presented in this work is the basis for the ultimate development of a beta-particle basket-catheter for the imaging of a damage myocardial tissue after an acute infarction. This kind of device would be a perfect reader for a tracer like the $^{18}$Fluorine-labelled Matrix Metallo-Proteinases [36], that is different taken up by healthy and damaged cardiac tissues.

The other SiPM based application investigated in this thesis, relates to the realization of a reader for dosimetric optical luminescence materials [37]. These are used in several fields: radiation dosimetry [38], clinical dosimetry [39], national security applications, luminescence dating [40] for geological [41] and archaeological samples [42]. OSL materials collect the dose received by ionizing radiations using electrons trapped in the imperfections of the lattice crystalline structure; these electrons are then released using light as stimulator; the amount of emitted light is proportional to the absorbed dose [43]. An OSL reader is based on two parts: the light stimulator and the light detector. Commercial (Risø Reader), and academic readers [44], [45],[46] are based on PMTs; so they are large and delicate instruments made only for laboratory measurements. Our innovative solution is a compact modular device based on the LED as stimulator and on the SiPM as the light photodetector, both with appropriate optical filters.

# 2 Silicon Photo Multiplier (SiPM)

SiPMs are the newest solid-state technology for photodetectors and they are replacing the PMTs in several different applications. SiPMs are the result of a long technology development, in which the goal was to build a solid-state photodetector with almost the same characteristics of a PMT. For this reason, a short review of PMT is necessary to continue our discussion about this new technology.

## 2.1 Photo Multiplier Tube (PMT)

The PMT (Figure 1) is an electronic detector of light, with high sensibility able to detect even a single photon in the UV, visible and near IR light range. A PMT is a vacuum glass tube, with one photocathode, one anode and some dynodes. Photons enter through an input window in the PMT and collide in the photocathode, which is covered by a material that allows photoelectric effect. The photocathode is a light sensitive surface that absorbs light and emits a proportional number of electrons, called photoelectrons.

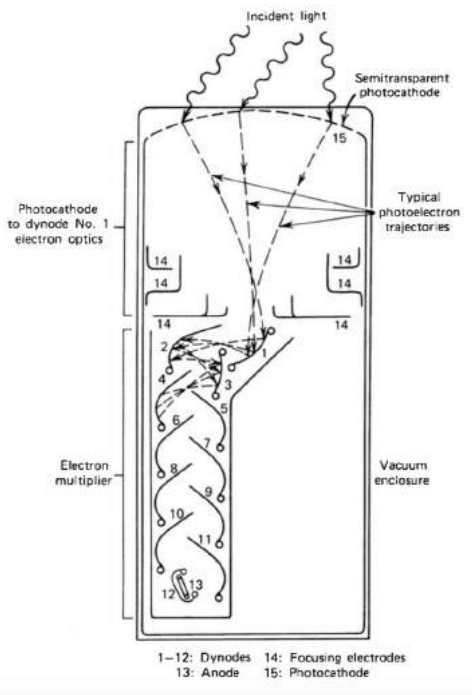


Figure 1: Scheme of a PMT [10].

The photoelectrons are focused by an electrode to the multiplication stage. This stage is made of an electrode series (dynodes), each one charged with an increasing

potential. Each photoelectron is accelerated by the electric field and acquires kinetic energy. When it hits the first dynode, other electrons are emitted (secondary emission); at the end of this cascade effect the generated electrons reach the anode, and an intense electric pulse is generated. This pulse is the proof of the photon detection.

Every dynode has a gain stage and the voltage between dynodes is one hundred volts. The number of electrons ($N_e$) that reach the anode depends on the number of incident photons ($N_{ph}$), the efficiency of the first stage ($\alpha$), the total gain (G) and the quantum efficiency (QE). The QE is defined as the ratio between the number of emitted photoelectrons and the number of incident photons [10]:

$$N_e = N_{ph}\, \alpha\, G\, QE \tag{1}$$

PMTs have to be magnetically shielded, in fact, an external magnetic field can modify the electron path inside the tube, producing an artifact in the response of the photomultiplier.

After a short review of PMTs an historical development of solid-state photodetectors is presented. In fact, SiPMs are the result of a long development history of solid state photodetectors, made to obtain results comparable with PMTs in terms of sensitivity, gain and more.

## 2.2 Historical development of solid-state photodetectors

The development of solid-state photodetectors went through several steps: the first one is the **Conventional Photodiodes** (PD) that only convert photons in electron-hole pairs, without internal gain; then the **Avalanche Photo Diodes** (APD), with an internal gain created by higher electric fields that increase the number of carriers; the **Single Photon Avalanche Diode** (SPAD) and finally the **Silicon Photomultipliers** (SiPM) that is an array of SPAD operating in Geiger mode. Before focus our attention to the SiPM, a short review of the previous technology is needed to better understand the newest one.

Conventional Photodiodes

A photodiode is a particular PN junction, with a strongly asymmetric doping; typically, the P region is more doped than the N one. A directly polarized photodiode has the same characteristics as a normal one, whereas an inversely polarized photodiode presents a depletion region width (w), given by the formula:

$$w = \sqrt{\frac{2\varepsilon(V + V_{bi})}{N\,q}} = \sqrt{2\,\rho\,\mu\,\varepsilon\,(V + V_{bi})} \tag{2}$$

in which ε is the dielectric constant, V is the external potential, $V_{bi}$ is the internal voltage, N is the doping-concentration, q is the electric charge, ρ is the resistivity and finally μ is the charged carriers mobility.

If incident photons deposit an amount of energy in the depletion region (Figure 2) greater than the difference between the material valence and conduction band gap, one electron-hole pair is created; the electron will move from the $P^+$ region to the N region because of the electric field, and the hole from N to $P^+$ region.

The loss of the e-h pair in the depletion region leads to the production of an inverse current, which can be read as an electric signal. The thickness of the depletion region determines the probability of photon interaction. The I-V characteristic curve (Figure 3) explains the photodiodes functionality: without photon interactions only dark current is present, while a real (photo-currents and dark current) signal is produced under photon exposure.

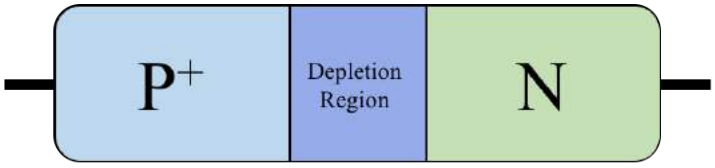


Figure 2: Photodiode scheme.

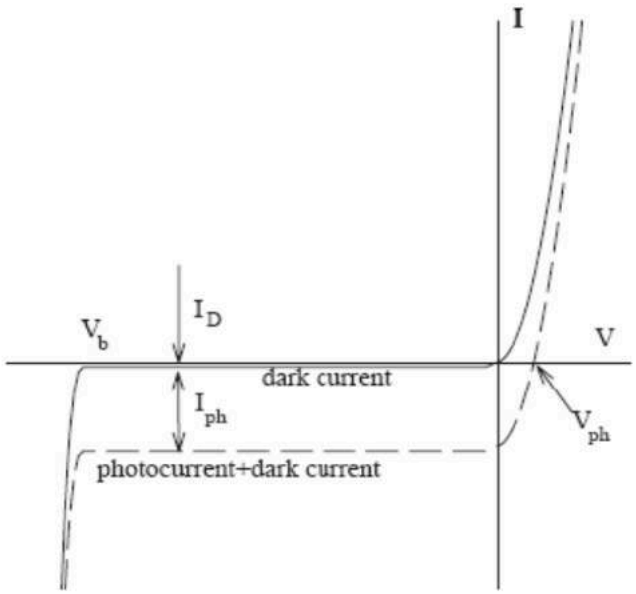


Figure 3: I-V characteristic of a photodiode.

The main photodiode technical characteristics are quantum efficiency and response: the former, as stated above, is defined as the number of e-h pairs created per incident photon, the latter is the ratio of photocurrent to incident optical power. The photodiodes have an internal gain in inverse polarization that is almost zero, so for low light level another step of development is required.

Avalanche Photodiodes (APD)

The APD structure is made of different doped semiconductor layers: $P^+$ region is a high concentration region of acceptor atoms, ND region is a no doping region, that keeps the electric field inside the junction almost constant, P region is a low concentration region of acceptor atoms and $N^+$ region is a high concentration region of donor atoms (Figure 4).

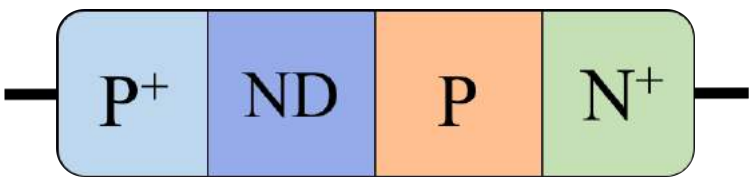


Figure 4: APD scheme.

The created primary charges pass through the P doped region and generate secondary charges, which will lead to a photocurrent. This avalanche phenomenon is strongly connected with the ND layer.

The main parameter of the APD is the multiplication factor (gain): it is the number of secondary e-h couples created for each primary couple. The APD gain increases with the inverse polarization, usually it has a value of $10^2$-$10^3$. Further development of APD is necessary if a higher gain is required

Singled Photon Avalanche Diodes (SPAD)

If high gain values are required, it is necessary to work in the upper limit of breakdown voltages, where the current increases exponentially. The SPAD is a normal APD that works in inverse breakdown mode, also called Geiger mode; in this case, also a single photon could be revealed. In Geiger mode, it is not possible to reveal another photon if an avalanche is still in progress: some quenching techniques are used to stop the avalanche phenomenon.

The main parameters of a SPAD are the Quantum Efficiency (QE) and the Detection Efficiency (DE)

$$\mathrm{QE} = \frac{\text{number of electron} - \text{holes pairs}}{\text{number of incident photons}} \tag{3}$$

$$\mathrm{DE} = \frac{\text{number of photoelectrons}}{\text{number of incident photons}} \tag{4}$$

After this short review of the previous solid-state detectors it is possible to explain what is a SiPM and how it works.

## 2.3 SiPM structure and characteristics

The SiPM is a pixelated device where each pixel, or microcell, is a combination of a single photon avalanche diode (SPAD) and a quenching resistor (RL) in series, with

all microcells connected in parallel, as shown in Figure 5. Typically, the dimensions of a SiPM microcell range from 10 μm to 100 μm, whereby the number of microcells per device depends on the application, and ranges from tens to several tens of thousands. The active areas of SiPMs typically range from 1 $mm^2$ to 6 $mm^2$ and their spectral response ranges from ultra-violet (UV) to near-infrared (NIR) [47].

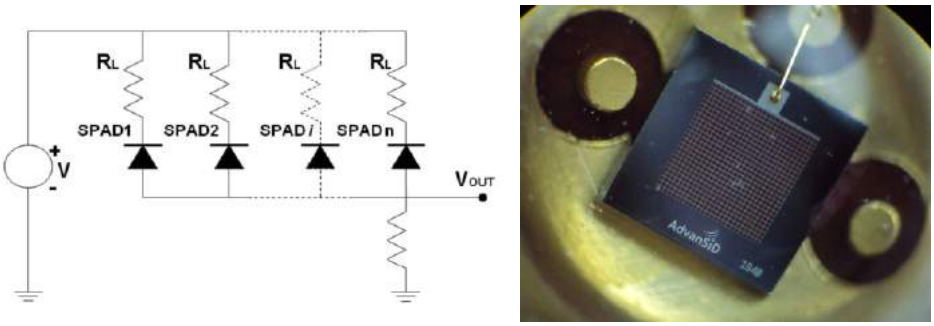


Figure 5: SIPM electronic schematic and a microscope image of the AdvanSiD SiPM.

A SiPM is externally biased so that the voltage on each SPAD is kept above the breakdown voltage. The difference between the biasing voltage and the breakdown voltage is known as overvoltage — the main adjustable parameter controlling the operation of the device. If a SiPM absorbs a photon, the resulting charge carrier (an electron or a hole, depending on the structure) can trigger an avalanche in the gain region. The avalanche can produce $10^5$-$10^6$ carriers, which constitutes the overall gain. The role of the quenching resistor is restoring the SPAD back to its initial state [48].

SiPMs are pixelated and thus recall a digital operation, however they produce an analog output signal in real time. The output is a time sequence of waveforms (or current pulses), which have a discrete distribution of amplitudes. The histogram of the amplitudes depends on the intensity and time-characteristics of the incident light [49]. The signal resolution of a SiPM allows resolving the number of photons hitting the device down to a single photon.

The photon detection efficiency (PDE) is the probability that a silicon photomultiplier (SiPM) will produce an output signal in response to an incident photon. It is a function of several factors: quantum efficiency (QE), probability of Geiger discharge ($P_{trig}$) and geometrical efficiency (GE). The quantum efficiency is the

probability that an incident photon will produce a charge carrier (electron or hole) capable of triggering a Geiger discharge. The geometrical efficiency, also known as fill factor, is the ratio between the active area and the total area of a SiPM [49]. The PDE can be expressed as follows [15]:

$$PDE = QE \times P_{trig} \times GE \qquad (5)$$

The dynamic range of a SiPM signal depends on the PDE and on the total number of microcells; the amplitude of the output signal is proportional to the intensity of the incident light when the number of photons hitting the device is much lower than the total number of microcells. Therefore, the dynamic range is limited by the number of available SPADs [15].

The SiPM time resolution depends on the rise time and the recovery time of the device. The rise time is the time required to produce a Geiger discharge, while the recovery time is required to return from the discharge back to the initial state. The timing properties of a SiPM depend mostly on the quenching resistor and on the diode junction capacitance [15]. A typical Geiger discharge is very fast (hundreds of ps), while the typical recovery time is the order of tents of ns [50]. The high time resolution of a SiPM allows several applications, including time of flight measurements in positron emission tomography (TOF-PET).

SiPMs present similarities with photomultiplier tubes such as the magnitude of the gain ($10^6$) and the high photon detection efficiency; however, SiPMs have some distinct advantages. The operational bias voltage of a SiPM is between 30 and 100 V, while a PMT requires around 1000 V [20]; therefore, a SiPM is characterized by a lower power consumption allowing the realization of compact multi-channel readout systems [51]. Moreover, SiPMs present better long-term stability and slower aging compared to PMTs [51]. Notably, SiPMs are insensitive to magnetic fields, and may be used inside magnetic resonance imaging (MRI) scanners, i.e., hybrid PET-MRI machines [52].

On the other hand, SiPMs also present some disadvantages compared to PMTs, like dark count rate (DCR), optical crosstalk and after-pulsing processes. Dark counts are the pulses observed in a device in the absence of light, and they are due to thermal processes occurring in the depletion region of the photodiode. The DCR increases with bias voltage and temperature. In applications where hundreds of photons are detected, the

DCR may be neglected, but for single photon measurements it must be corrected for. Optical crosstalk occurs when a primary discharge (avalanche) in a microcell triggers secondary discharges in one or more adjacent microcells. The secondary discharge may be nearly simultaneous with the primary (direct or prompt crosstalk) or delayed by several tens of nanoseconds (delayed crosstalk). If not corrected for, crosstalk makes the output signal higher than that due to the incident light. After-pulsing processes are caused by signal carriers trapped in silicon defects during the avalanche phenomenon: the trapped carriers are released during the recovery phase, producing a secondary pulse in the output signal [15].

Like a photomultiplier tube, a SiPM can operate in two distinct modes: continuous wave and photon counting. In the former, the output pulses are not counted individually; instead, an analog output current is recorded. In the latter, the individual pulses are either counted (digital photon counting) or integrated to yield the charge released in the Geiger discharge (analog photon counting). The choice of operation mode depends, among other factors, on the frequency and duration of the output pulses. When pulses are frequent and overlapping, the continuous wave mode is appropriate. When pulses are distinguishable, then photon counting — analog or digital — is preferable.

A recent development of the SiPM technology was the introduction of the digital SiPM (dSiPM). In dSiPMs, photons are counted as digital signals using an electronics cell for each SPAD, containing active quenching, one bit memory and recharge circuits ( Figure 6). These new devices are less sensitive to electromagnetic interference and temperature variations, and they require a simpler readout front-end [53].

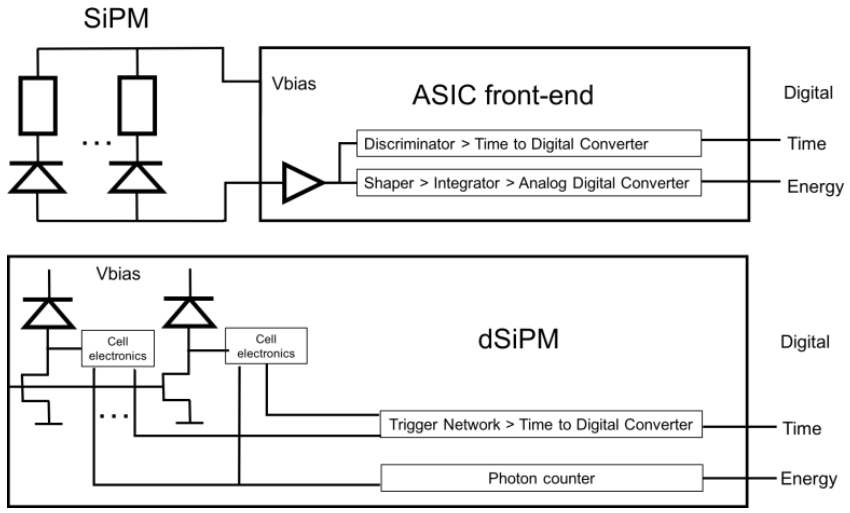


Figure 6: Comparison between SiPM and dSiPM.

The performance of SiPMs is affected by damage caused by ionizing radiation: the main effect induced by exposure to ionizing radiation is an increase in DCR. This increase is more of a concern for single photon measurements, while it may be usually neglected for high intensity light measurements. Therefore, irradiated SiPMs must be accurately characterized in terms of DCR and other parameters [54]. In dSiPMs, the prevalent damage is again in the SPAD and not in the integrated electronics. If a cell in a dSiPM is damaged by radiation, it can be individually disabled to limit the effect on the performance of the device [55].

## 2.4 SiPM front-end

The analog front-end circuit for a SiPM is usually a trans-impedance amplifier (Figure 7) which converts and amplifies the output current into a voltage. This stage has a trans-impedance gain which is a function of $R_f$, and it is usually followed by other stages to further amplify the signal when required by the application.

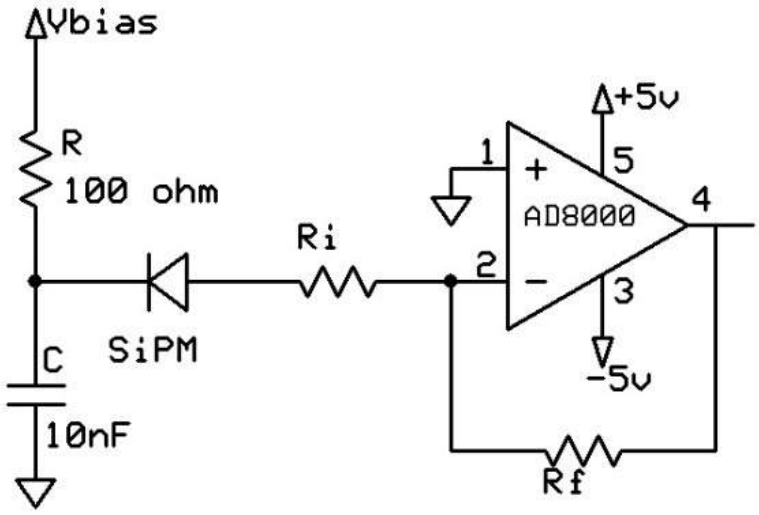


Figure 7: Circuit diagram of the trans-impedance amplifier connected to a SiPM.

The features of the SiPMs described in the previous chapter are the reason for their wide acceptance and range of applications. These photodetectors are compact and very powerful devices, capable of detecting low light intensities corresponding to a single photon. The devices are highly customizable, since the number of micro-cells can be chosen in relation to the specific application, e.g., in relation to the required active area. Great opportunities are offered by their ability to detect light at low optical intensities with an efficiency comparable to PMTs combined with the insensitivity to magnetic fields typical of semiconductors. Further opportunities will be offered by dSiPMs, which are already commercially available and are currently undergoing extensive validation studies. An important concern to be addressed is their resistance to ionizing radiation damage, which is especially relevant when high-energy neutrons or cosmic radiations are measured [56, 57].

# 3 State of the art of SiPM applications

SiPMs are a new type of solid-state photodetector, based on a matrix of APDs working in GM; they are very promising detectors for low light measurements, thanks to their stability and high internal gain. SiPMs are the modern substitute of PMT, they show a lot of advantages like for example lower power consumption, compact size, stronger to mechanical vibration and temperature changes, insensitive to magnetic fields and a higher quantum efficiency [15]. One of the first application was replacing the PMT in the scintillation detectors like calorimeter [50].

SiPMs are already used in a large varieties of different application fields. The majority of these applications can be divided in two categories: biosensing and radiation detectors. The first category illustrates the full potential of SiPMs in applications that usually require miniaturization down to the micrometer scale, as well as the need for the highest radiation sensitivity. On the other hand, in radiation detection, when micrometric dimensions are less important, characteristics such as ultra-fast rise and fall times, as well insensitivity to magnetic fields offer SiPM a significant advantage over conventional PMTs.

## 3.1 SiPM in biosensing

A biosensor device can be defined as the integration of different components such as fluidics, electronics, separation technology, and biological subsystems applied to a biological model [1, 58]. Different categories of a biosensor are presented in Figure 8. If light is the physical quantity transduced by the electronic component of such device, then we have an optical biosensor [59].

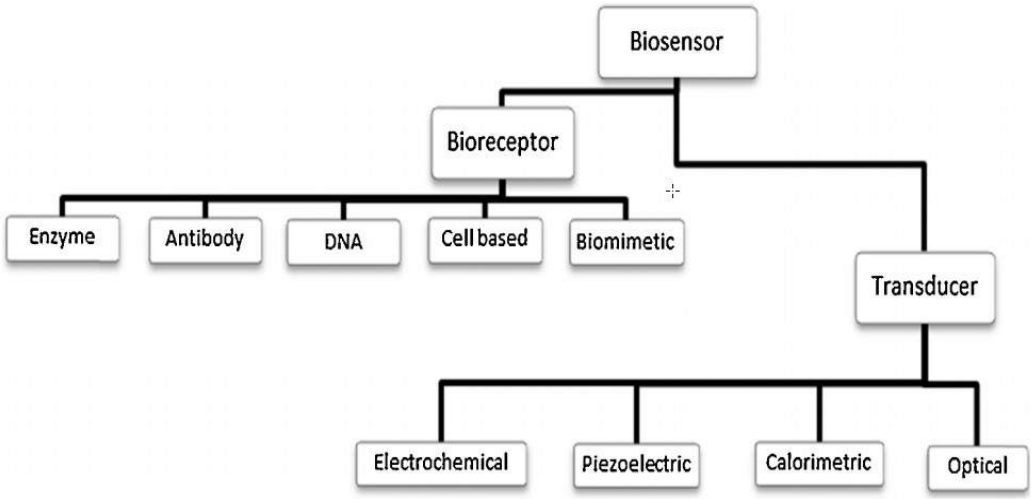


Figure 8: Different categories of biosensor [1].

A SiPM could be integrated as the electronic part of a biosensor acting as the optical transducer which is able to detect small changes in the absorbance, luminescence, polarization, or refractive index between the reactants and products of a biological subsystem reaction [60, 61].

Bio-luminescence and light scattering methods are optical methods used by biosensors, that have been proven to be the most effective methods in the field of bioimaging research [62, 63], on the other hand, the collection of photoluminescence is very difficult due its extremely low intensity, typically in the order of a micro-lux [64, 65]. Consequently, the challenge associated to collecting of these optical signals with sufficient signal-to-noise ratio is enormous.

Several studies have shown that using a SiPM as a readout device provides an adequate performance [66, 67] combined with micrometer dimensions, as shown in Figure 9, that are also required for biosensors [29, 68].

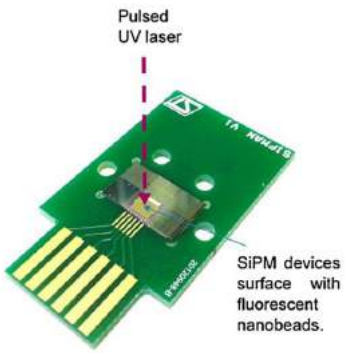


Figure 9: Prototype device of an integrated fluorescence-based microarrays [67].

Indeed, a recent study (Figure 10) revealed that a simple, low cost and portable optical system, with a SiPM optical transducer, is able to detect fluorophore concentrations in the order of $10^{-12}$ M. SiPMs are able to detect very low level of fluorescence and show a linear response for two different molecular biotechnology: the DNA microarray and the real time polymerase chain reaction [30].

Another application of SiPM in biosensing is the measurement of adenosine triphosphate (ATP). In Figure 11 there are the particular of the SiPM (a), the measurements scheme (b), the 3D printed microfluidics chip scheme (c) and the image of the real device (d).

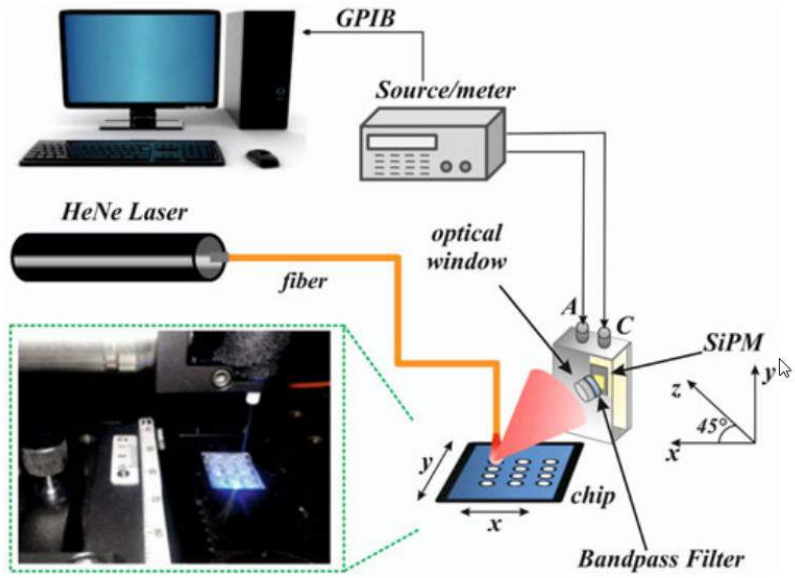


Figure 10: Experimental setup for liquid samples characterization [30].

Thanks to the SiPM innovative technologies a miniaturized bioluminescence sensing system is been developed and tested with positive result. In this proposed solution SiPM is the key part of the project not only for its miniaturized characteristics and high sensitivity but also because it simplifies the signals analysis compared with the traditional image off-line analysis. In this work, the dynamic range of the SiPM biosensor is compared with a PerkinElmer commercial reader with great results. Moreover, this real-time solution allows to monitoring biological events without perturbing the system [29].

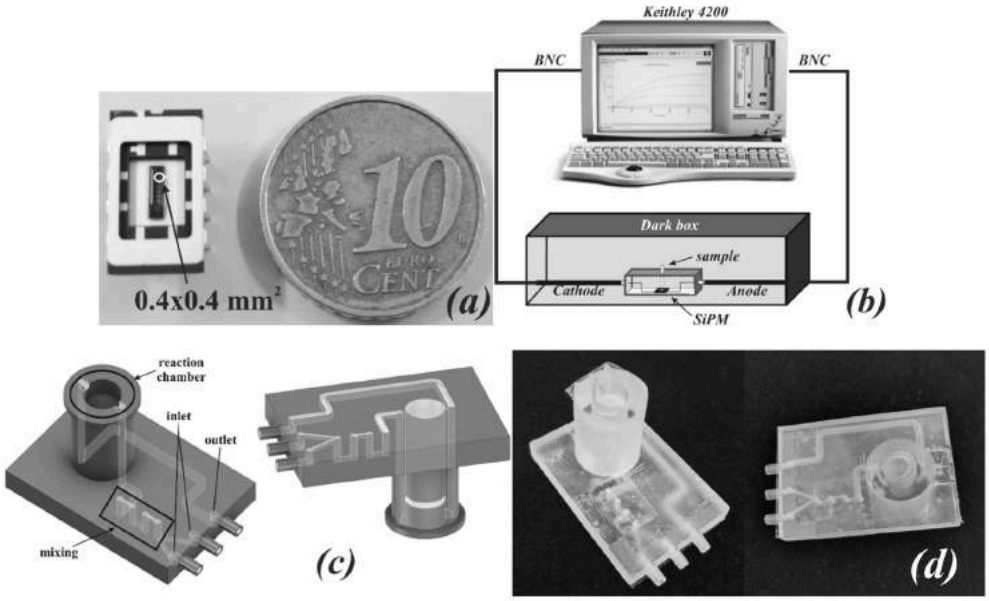


Figure 11: Experimental setup for ATP bioluminescence detection [29].

Due to all SiPM described characteristics, it is expected that promising applications will emerge in biosensing research by using SiPMs as optical transducers instead of the conventional photodetectors.

The biosensing is not the first field of application in which SiPM have changed the way to measure low level light; in fact, the first application was in a complete different field the nuclear measurement, where SiPM has started to replace the traditional PMT in the scintillation detectors.

## 3.2 SiPM in scintillation detection

Before analyzing the state of art of SiPM used as scintillation light detectors, it is important to review the general features of scintillation detectors in general. A scintillation detection system consists mainly of 3 components (Figure 12): first, when ionizing radiation interact inside a scintillator, the light emitted is proportional to the energy absorbed by the medium; then, a photomultiplier unit amplify and convert the light into an electric signal, which is digitized by an electronic data acquisition board.

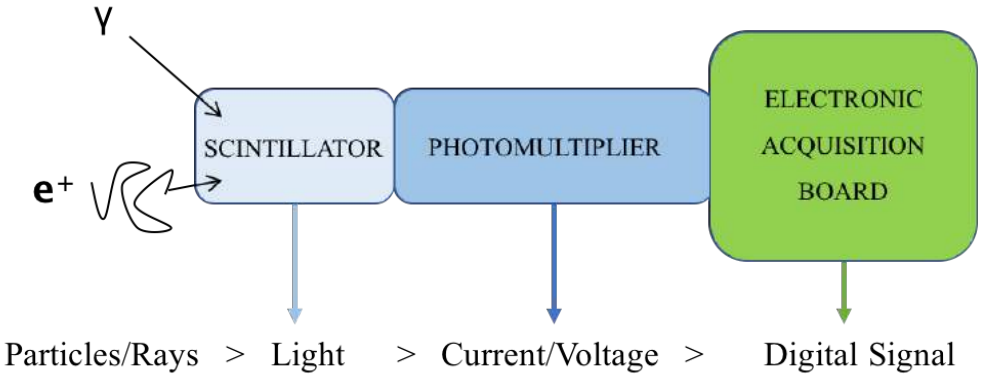


Figure 12: Architecture of a scintillation detection system: the device is mainly composed by the scintillator, the photomultiplier and the electronics acquisition board.

The scintillator materials are classified in two main categories (based on their chemical composition and emission process): inorganic scintillator (Na(Tl), Cs(Tl), BGO, LYSO, etc.) [69] and organic scintillator (plastic, PVT, anthracene, etc.).

Regarding the choice of the photomultiplier unit, two main types are available: the traditional PMT and the new semiconductor based photomultiplier the SiPM.

The first SiPM application in nuclear radiation measurements has been in scintillation detectors [70], and this is still the main application nowadays [71, 72]. Using SiPMs optically coupled with an inorganic scintillator, such as CsI:Tl, it possible to realize a gamma spectroscopy system with the same energy resolution characteristics as the PMT-based systems [73]. SiPMs are used in various high energy physics measurements, such as in calorimetry. For this reason, some studies have analyzed the damage threshold of the SiPM exposed to high energy gammas up to 6.1 MeV [57, 74], revealing that these photodetectors, besides the characteristics described above, also have a higher energy damage threshold, making them even more suitable for this type of research.

Now that their accuracy and energy resolution have been verified, SiPMs are starting to replace PMT in various fields of application of scintillation detectors such as environmental radiation monitoring [75] and even in portable fast detectors for radon [76]. Portable SiPM based dosimeters have also been described for measurements of ambient dose equivalent $H^*(10)$ with CsI(Tl) scintillators, which require a method to correct for their non-tissue equivalence [77]. SiPM photodetectors have also been tried for neutron detection where area monitors such as the "Rem counters" are often complex, expensive and bulky. It is possible to overcome those limitations using a SiPM combined with a

LiI(Eu) scintillator [78]. Recent application have shown that it possible to build an ultra-thin (1.5 mm) neutron detector with a SiPM, a WLS coupled to a $^{6}$LiF:ZnS(Ag) scintillator and using pulse shape discrimination to achieve an effective gamma ray rejection [79].

The compactness, robustness and low bias voltage of SiPMs are also ideal for the development of personal radiation sensors; moreover, SiPMs are relatively inexpensive and are an affordable choice for devices to be assigned to a large number of workers. For homeland security applications SiPMs are a suitable solution to develop a personal radiation detector; for example, the SENTIRAD, based on SiPM coupled with a CsI(Tl), was proven to be a good solution for this kind of application [80].

SiPMs are suitable to be used also in medical radiation detection applications. Using SiPMs coupled with scintillating optical fibers in coincidence mode [81], it is possible to achieve a radiation dosimeter for low dose rates, such as those emitted by an X-ray tube with anode currents of a few μA, overcoming the dark count rate limitations by using two SiPMs. Beta particle detection has been examined in relation to the development of intraoperative or endovascular radiation probes which will help detect and map the differential uptake of positron emitting tracers and thus localize tumor tissue or damaged cardiac tissue [34, 36]. Indeed, detecting the exact position of a tumor target is fundamental in cancer therapy in order to improve the efficiency of cancer removal and to avoid relapse of the disease. Using a probe for beta particle emitting radiotracers has been found to increase the spatial resolution by a factor of 4 in the determination of the tumor position, compared to a gamma sensitive probe [82]. SiPMs are probably the best solution for the development of similar intraoperative beta particle probes [34].

Current marketing of SiPMs by several manufacturing companies, such as Hamamatsu, SensL, AdvanSid, and Ketek, leads to continuous, rapid improvements in the performance of these photodetectors. A recent and extensive compared investigation [83] has shown that the PDE from the commercialized SiPMs is similar to all tested brands, whereas the pulse shape, DCR, and the time transit delay show significant changes. The synergy between research and industry allows SiPMs to be widely used in nuclear medicine, in particular in equipment such as Positron Emission Tomography (PET) and Single-Photon Emission Tomography (SPECT) [84]. In these applications, SiPMs are built as large area detectors with multichannel data acquisition as well a

dedicated front-end preserving the quality of signals acquired over a multitude of channels [53, 85]. Due to the insensitivity to magnetic interference, SiPMs can be used inside strong magnetic fields such as those up to 7 T used in Magnetic Resonance Imaging (MRI) [86, 87]. Another recent application which combines a SiPM and nuclear medicine is the single-photon emission computed tomography (SPECT), called SPECT/MRI [88]. The fast rise and decay times of SiPMs also allow the adoption of these photodetectors in techniques requiring time resolutions in the order of $10^{-10}$ s, such as TOF-PET [35, 89, 90].

# 4 Development of a beta detector based on plastic scintillator and SiPM

*"The detection of ionizing radiation by the scintillation light produced in certain materials is one of the oldest techniques on record" [10]*

*GLENN F. KNOLL*

One of the first SiPM application, in nuclear radiation measurements was in scintillation detectors, and this is still the main application nowadays. In short, a scintillator is an organic or inorganic compound that absorbs ionizing radiation and emits light proportionally to the amount of absorbed energy. Beta particle detection has been examined in relation to the development of intraoperative or endovascular radiation probes mapping the differential uptake of positron emitting tracers. SiPMs are arguably the best solution for the development of these probes since they are small and require a low-voltage bias. In this chapter, a beta probe was developed using a SiPM optically coupled with a plastic scintillator, in order to fully understand the behavior of this new scintillation detector.

## 4.1 Characteristics of the Beta Probe

The Beta Probe (BP), a lab-made detector, was created using a SiPM model ASD-NUV1S-MG from AdvanSiD Company (Figure 13).

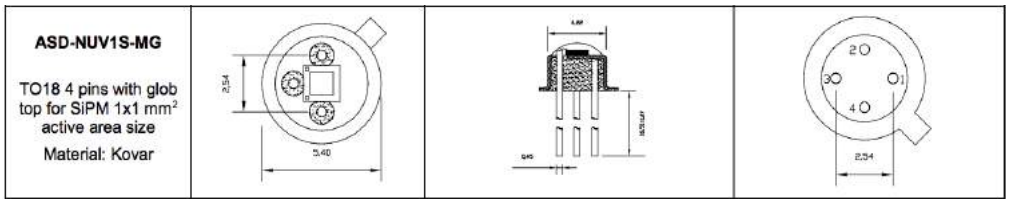


Figure 13: AdvanSiD SiPM (ASD-NUV1S-MG) scheme.

AdvanSiD ASD-NUV SiPMs are based on the AdvanSiD P-N silicon technology for detection of Near Ultraviolet light (NUV). NUV-SiPMs have peak efficiency at 420nm, with detection spectrum extending from 350nm to 900nm with an active area of $1mm^2$ (Figure 15).

The SiPM (Figure 14 a, b) was coupled with a plastic scintillator (polipop 0180) (Figure 14 c). A perfect optical coupling is required to collect all the light produced by the scintillator. Optical coupling between scintillator and SiPM was achieved with an optical glue (Meltmount) and carefully avoiding the inclusion of microscopic air bubbles that may affect the refractive index.

The SiPM coupled with the scintillator (Figure 14 d) was wrapped with multiple layers of white PTFE tape (Figure 14 e), in order to reflect scattered light and collect as much as possible of the light yield.

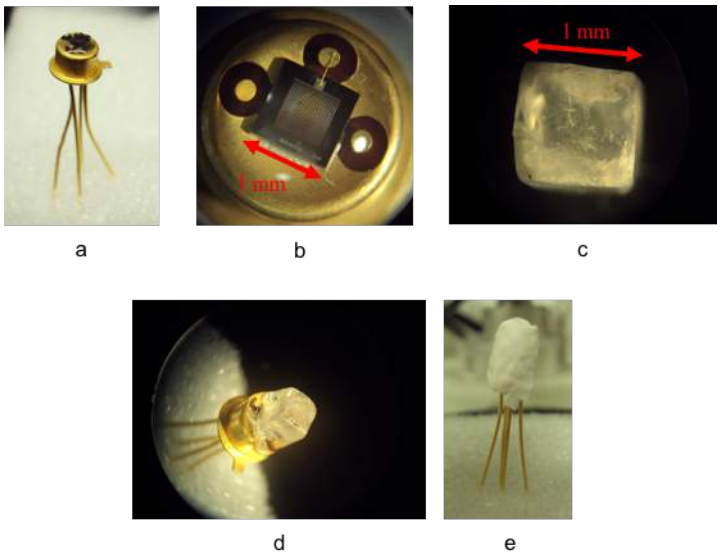


Figure 14: (a, b) AdvanSiD SIPM, (c) plastic scintillator, (d) SiPM coupled with scintillator, (e) wrapped couple.

| Symbol | Parameter | Product | | | |
|---|---|---|---|---|---|
| | | ASD-NUV1S-M/MG | ASD-NUV1C-M/MG | ASD-NUV3S-M | ASD-NUV4S-M |
| AA | Effective active area | 1×1 mm$^2$ | 1.13 mm$^2$ | 3×3 mm$^2$ | 4×4 mm$^2$ |
| N | Cell count | 625 | 673 | 5520 | 9340 |
| CS | Cell size (pitch) | 40 µm × 40 µm | | | |
| FF | Cell fill-factor | 60 % | | | |
| RQ | Quenching resistance | 800 kΩ | | | |
| C | Cell capacitance | 90 fF | | | |
| $\tau_{RC}$ | Recharge time constant | 70 ns | | | |
| $S_R$ | Spectral response range | 350 to 900 nm | | | |
| $\lambda_p$ | Peak sensitivity wavelength | 420 nm | | | |
| PDE | Photon Detection Efficiency (1) | 43 % | | | |
| BV | Breakdown voltage(2) | Typical: 26 V | | Min: 24 V | Max: 28 V |
| σBV | BV standard deviation(3) | 50 mV | | | |
| OV | Recommended Overvoltage range(4) | Min: 2 V | | Max: 6 V | |
| DCR | Dark Count Rate(5) | < 50 kHz/mm$^2$ @ 2 V OV | | < 100 kHz/mm$^2$ @ 6 V OV | |
| G | Gain(6) | 3.6×10$^6$ | | | |
| BVTC | Breakdown Voltage Temperature Coefficient | 26 mV/°C | | | |

(1) Measured at peak sensitivity wavelength ($\lambda = \lambda_p$) at +6 V overvoltage (not including afterpulse and crosstalk).
(2) Refer to the data provided with each shipped product.
(3) BV of SiPMs belonging to a same production lot is within 200 mV ($\pm 2\sigma$) from mean BV value.
(4) Operating voltage (SiPM bias) is BV + OV, to be applied in reverse mode, i.e., $V_{AK} < 0$ (see "Pins Function" section).
(5) 0.5 p.e. threshold level at 20 °C (primary dark count rate; not including afterpulse).
(6) Measured at 20 °C at +6 V overvoltage.

Figure 15: AdvanSiD ASD-NUV SiPM datasheet.

The AdvanSiD SiPM was connected to a dedicated, high performance AdvanSiD evaluation board (mod. ASD-EP-EB-N) (Figure 16).

The board has been specifically designed to match and optimize the performances of AdvanSiD SiPMs. It represents the most suitable way to use AdvanSiD detectors.

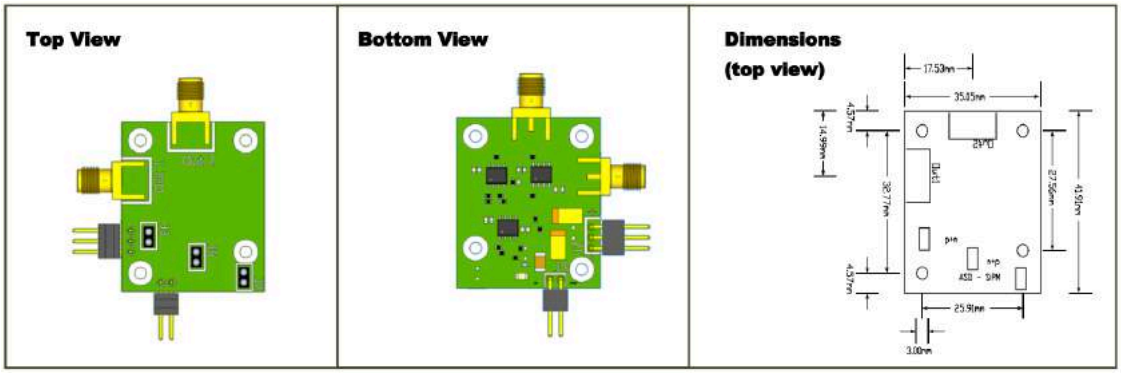


Figure 16: ASD-EP-EB-N geometric specifications.

impedance amplifier stage (Z = 1000 Ω) followed by two independent output stages (Figure 17). OUT 1 provides a buffered output with a total trans-impedance gain G1 = 500 Ω when terminated on a 50 Ω load. OUT 2 provides a further non-inverting amplification stage with a gain of 5 that gives a total trans-impedance gain G2 = 2500 Ω when terminated on a 50 Ω load.

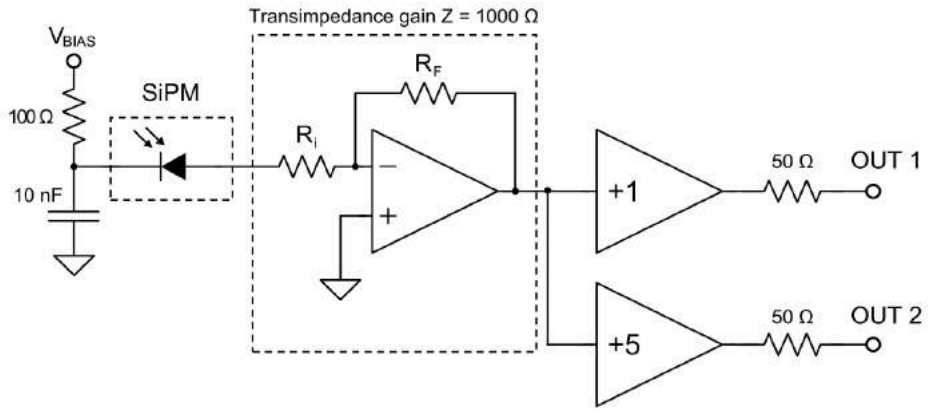


Figure 17: ASD-EP-EB-N schematic.

The board requires a stabilized dual power supply (+5 V/-5 V), which is made with a TDK-Lambda KMD40-55. Another single power supply (0/+30 V) is required to bias the SiPM.

A mechanical and electronic support for the board (Figure 18 a) and the SiPM was designed (Figure 18 b); since it is very important to avoid the environmental light contamination, the enclosure was realized using a light tight plastic case (Figure 18 c).

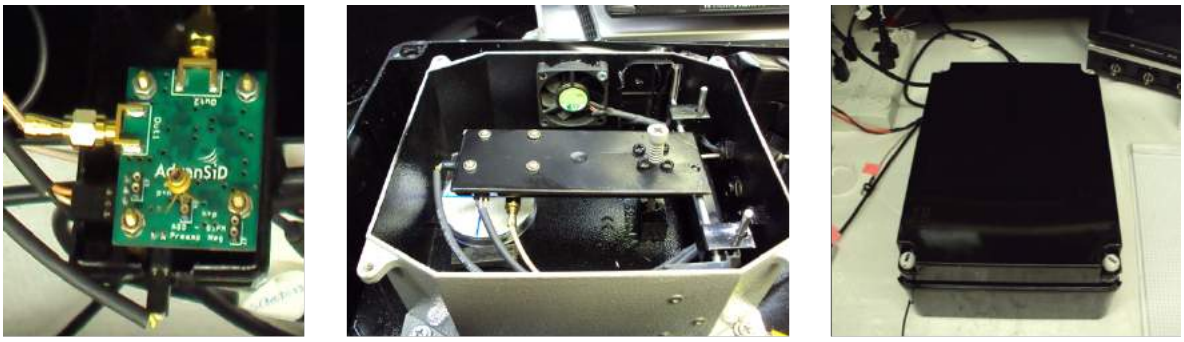

a b c

Figure 18: Beta probe first prototype.

In all the preliminary tests, the output signal from electronic board was collected with an oscilloscope Lecroy Waverunner 6zi; the scope creates a histogram, visible on the right part of

Figure 19, based on the integrated areas under the signals, using the internal multi-channel analyses (MCA). A SiPM current check was performed in advance to verify if the I-V characteristic curve was the same as the one reported in the datasheet.

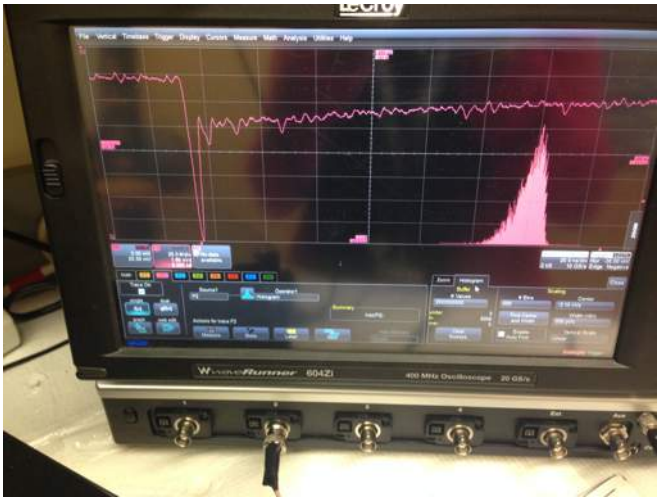

Figure 19: First beta probe measurements with the oscilloscope.

A preliminary study verified the response of the lab-made system using radioactive sources: in absence of the source, the system produced only a baseline signal; with the presence of the source, the response of the system showed the typical signal of a scintillator device.

Several tests were done before the measurements, in order to set the optimal bias voltage of the SiPM and the trigger voltage level to reject the noise signals.

The goal for every measurement was to achieve at least 10,000 counts. This value, considering the Poisson statistics followed by nuclear detection systems, yields a relative standard deviation in the order of 1%.

Two kinds of measurements were performed: a beta attenuation measurement and a beta spectrum analysis.

To perform both studies we used two types of radioactive sources:

- Beta and gamma solid sources (Figure 20): $^{90}$Sr that is a pure beta emitter and $^{137}$Cs that is a beta/gamma emitter.


a b

Figure 20: (a) Radioactive source $Sr^{90}$, (b) $Cs^{137}$ used in beta detector measurements.

- Liquid beta source on paper filters (
- Figure 21): fludeoxyglucose ($^{18}$F-FDG)

Figure 21: $^{18}$F-FDG paper filter samples used in beta detector measurements.

To develop a complete and compact probe, a suitable analog to digital converter was necessary to replace the oscilloscope used in the first tests; therefore, a DRS4 board (Figure 22) made by Paul Sherrer Institute (PSI, Switzerland) was chosen as the best solution to replace the oscilloscope. This board is based on a FPGA chip, allowing GSPs acquisition speed.


Figure 22: PSI DRS4 evaluation board.

The output of the board is a binary code that required a specific self-made software written in Matlab in order to use the data and create the histogram spectrum. From the table (Figure 23) present in the manual a translator code was developed capable to save the header file and the measurement file (time and voltage).

| Word | Byte 0 | Byte 1 | Byte 2 | Byte 3 | Contents |
|---|---|---|---|---|---|
| 0 | 'D' | 'R' | 'S' | '2' | File header, Byte 3 = version |
| 1 | 'T' | 'I' | 'M' | 'E' | Time Header |
| 2 | 'B' | '#' | Board number | | Board serial number |
| 3 | 'C' | '0' | '0' | '1' | Channel 1 header |
| 4 | Time Bin Width #0 | | | | Effective time bin width in ns for channel 1 encoded in 4-Byte floating point format |
| 5 | Time Bin Width #1 | | | | |
| ... | ... | | | | |
| 1027 | Time Bin Width #1023 | | | | |
| 1028 | 'C' | '0' | '0' | '2' | Channel 2 header |
| 1029 | Time Bin Width #0 | | | | Effective time bin width in ns for channel 2 encoded in 4-Byte floating point format |
| 1030 | Time Bin Width #1 | | | | |
| ... | ... | | | | |
| 2052 | Time Bin Width #1023 | | | | |
| 2053 | 'E' | 'H' | 'D' | 'R' | Event Header |
| 2054 | Event Serial Number | | | | Serial number starting with 1 |
| 2055 | Year | | Month | | Event date/time 16-bit values |
| 2056 | Day | | Hour | | |
| 2057 | Minute | | Second | | |

Figure 23: PSI DRS4 binary conversion table.

**Beta attenuation measurements**

During these measurements, the device response to the same radioactive source was calculated using several polycarbonate layers (ρ=1.2 g/cm3, t=1.5 mm) to shield the device (Figure 24); by increasing or decreasing the total thickness of the layer between the source and detector, we obtained the absorption curves (the number of electrons that crossed the matter thickness as a function of the thickness). Measurements were made without any layers of plastic, and then one layer added one by one.

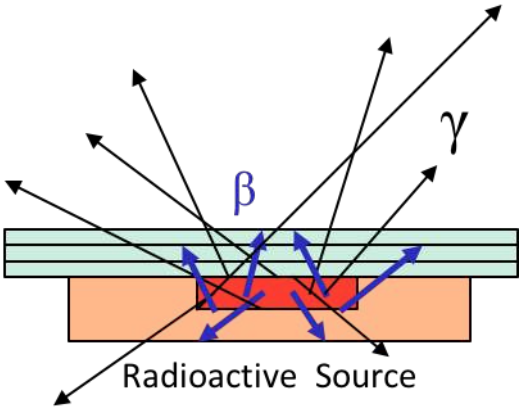


Figure 24: Source scheme during the attenuation measurements.

The set-up used for the measurements (Figure 25) was made using a lab-made 3D printed support (on the right part of Figure 25); this strategy allowed to achieve the same geometry for every measurement.

In fact, the sources were mantaneid in the same marked position and the distance between sources and probes was fixed at 9 mm (corresponding to 6 pieces of polycarbonate PC).

The same power supply (Vbias = 26 V), which determines the gain of the SiPM, was used in order to compare the data acquired during the tests. All the measurements are normalized against the time.

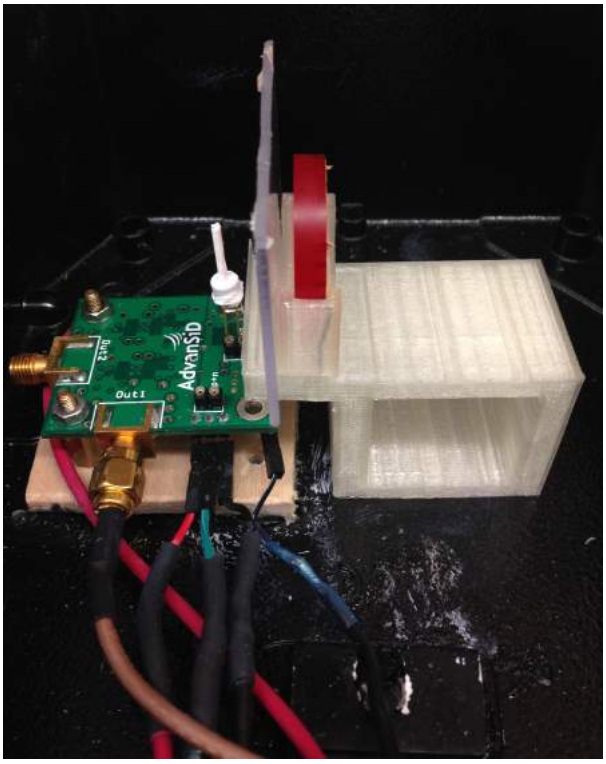


Figure 25: Attenuation set-up used in beta detector measurements.

The number of counts through the material depth determines the absorption curve, in which the maximum depth is called maximum range ($R_{max}$). One typical example of this curve is reported in Figure 26.

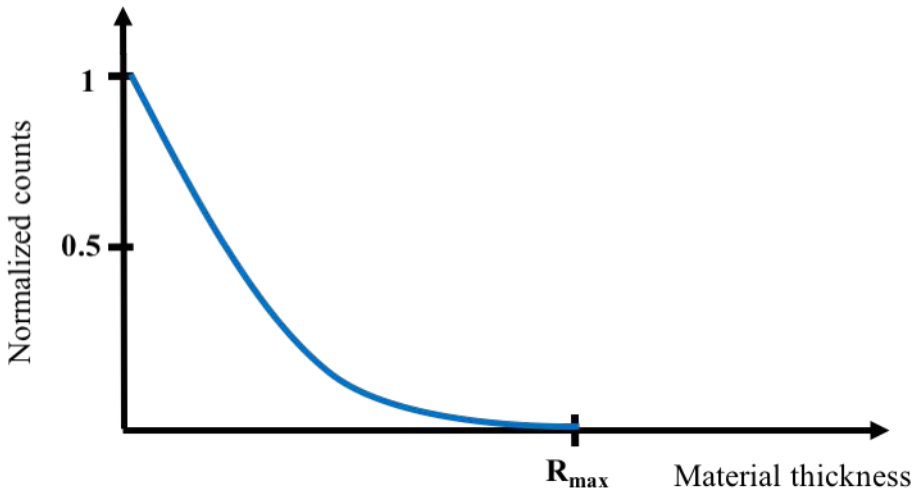


Figure 26: Typical beta absorption curve.

This value is related with the beta maximum energy. There are several methods to calculate the $R_{max}$ based on semi-empirical equations, one of most accepted one is the followed relations [91]:

$$R_{max}\left(\frac{mg}{cm^2}\right) = 412\,E^n \qquad 0.01\,MeV < E < 3\,MeV \qquad n = 1.265 - 0.0954\,ln(E) \tag{6}$$

$$R_{max}\left(\frac{mg}{cm^2}\right) = 530\,E - 106 \qquad 1\,MeV < E < 20\,MeV \tag{7}$$

**Beta spectrum analysis:**

An energy spectrum is measured using the detector in *pulse mode operation*, in which each radiation quantum gives rise to a distinguishable signal pulse. This kind of detection mode allows measuring the energy distribution of the incident radiation (spectroscopy analysis). Indeed, the analysis of the pulse amplitude gives information about the charge generated by the radiation interaction in the detector.

The subtended area of each pulse produced by the detector (Figure 27) is collected in the histogram on Figure 27 b, in which the height of each column is related to the number of pulse with the same amount of area. The area of the pulse is proportional to the energy release by the radiation on the detector.

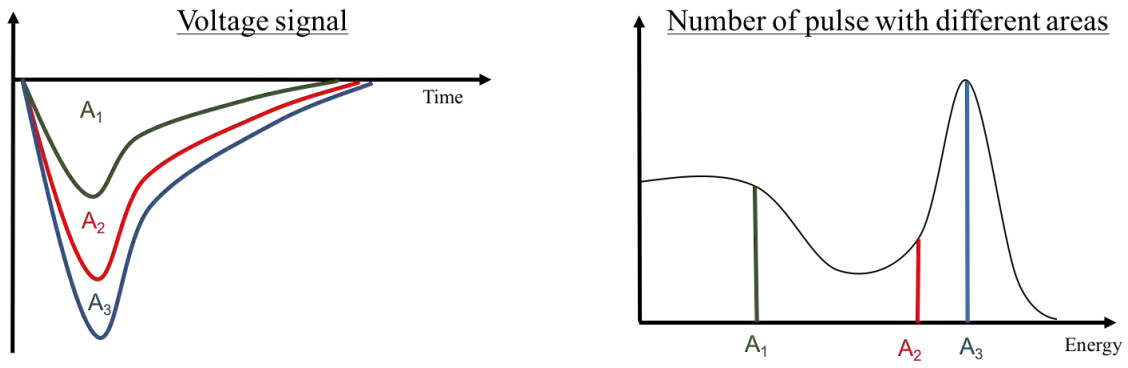


Figure 27: Spectrum analysis.

Spectra are collected by applying the MCA theory, using the calculated area, measured in volt for seconds (Vs) above the SiPM pulse curve obtained by the oscilloscope. This allow to choose the threshold and create the counts histogram.

## 4.2 Result and discussion

The results obtained with the BP probe (Figure 28) are consistent with the known beta attenuation behavior: for a beta source like the $^{90}$Sr the absorption curve is a pseudo-exponential as we say in the previous paragraph and the maximum range (for the 2.2 MeV particles) is 9.1 mm as it expected from the previous semi-empirical formula.

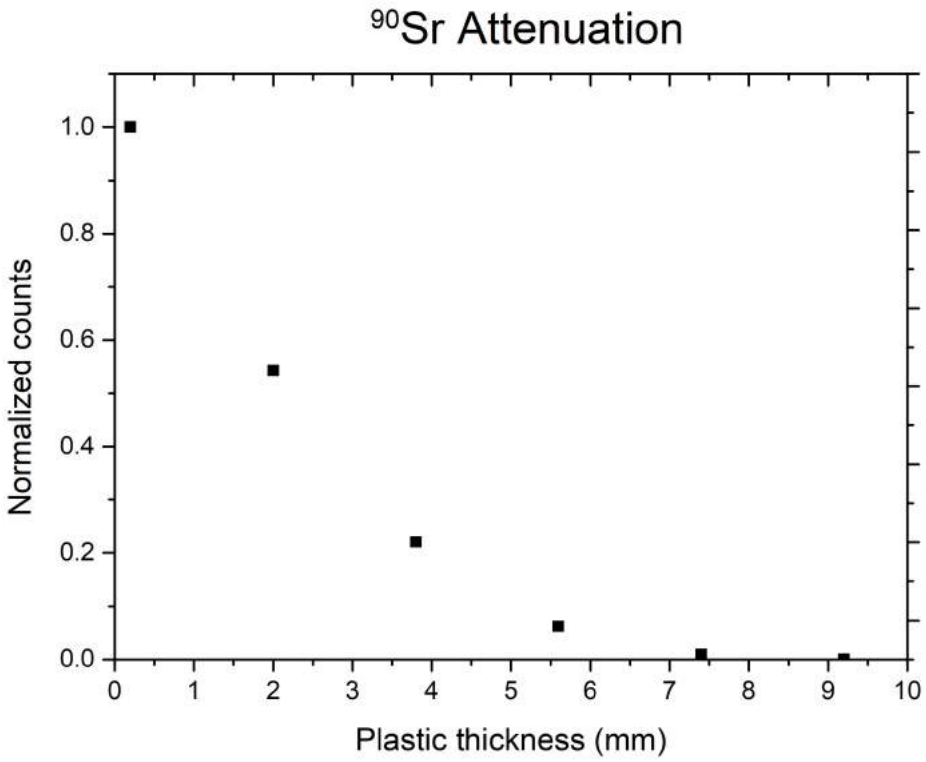


Figure 28: Experimental $^{90}$Sr attenuation curve obtains with the BP probe.

The $^{137}$Cs attenuation measurements confirm the same correct behavior of the probe and also allow to see another phenomenon. The beta particles range for the 0.512 MeV from $^{137}$Cs is 1.41mm less than 1 layer of polycarbonate. So only one polycarbonate layer is enough to stop all that beta particles. This phenomenon is clearly visible in the graph (Figure 29) for the BP probe. Only in the first two point there are beta particles,

whereas only gamma rays are detected in the other. This is a correct behavior compatible with the range of the particles. Another observation is that the probe is capable to measure also gamma rays because after the attenuation of the beta particles the numbers of count does not go to zero as for the $^{90}Sr$ that is a pure beta source. So, the attenuation curve from the third point is a real exponential.

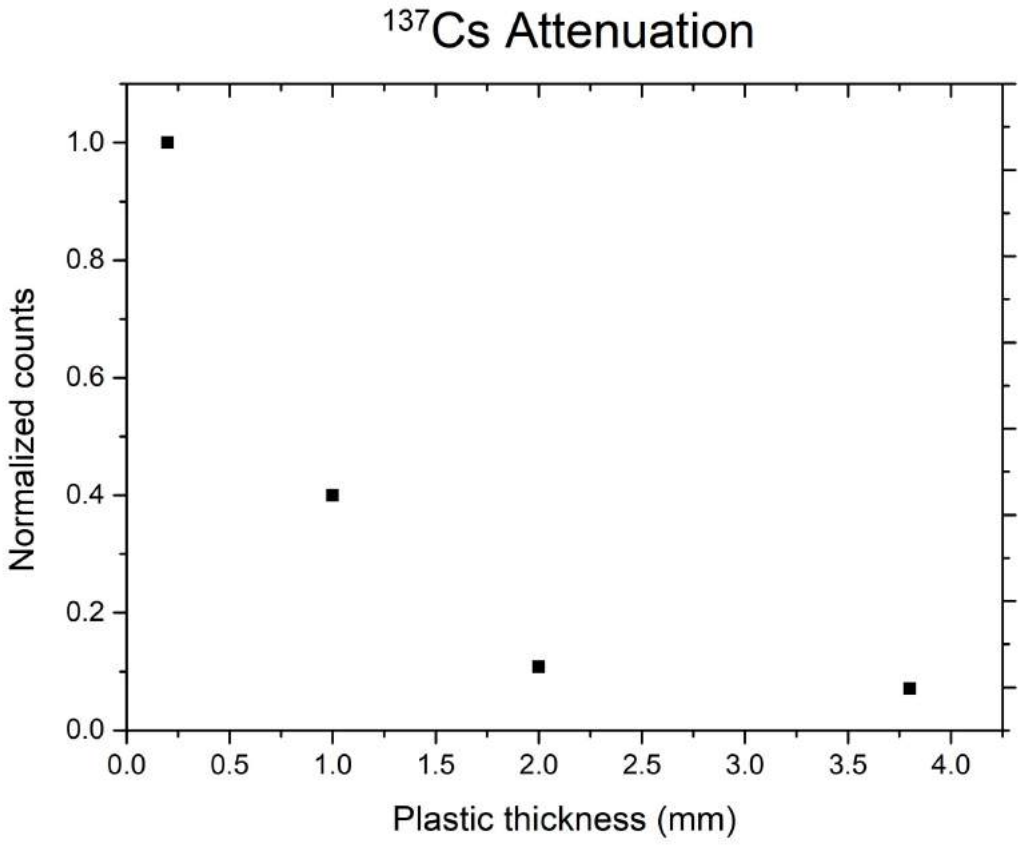


Figure 29: Experimental $^{137}Cs$ attenuation curve obtains with the BP probe.

The experiment with $^{18}F$-FDG (Figure 30) on paper filter confirms that the response to the $^{137}Cs$ is very similar to the $^{18}F$-FDG, because these two sources emit gamma radiation of similar energy (annihilation photons for the $^{18}F$-FDG and 662 keV for the $^{137}Cs$) and beta particles with close energies: 624 keV for the $^{18}F$-FDG and 512 keV for the $^{137}Cs$ as maximum beta energies.

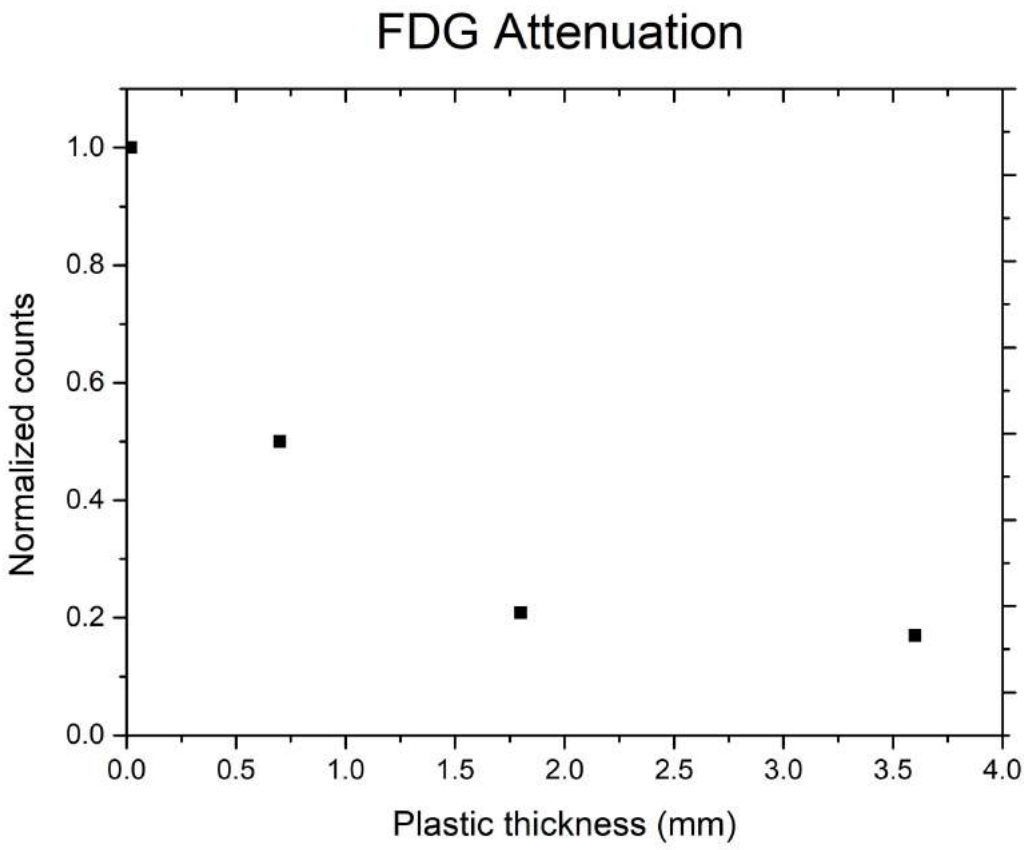


Figure 30: Experimental FDG paper filter attenuation curve obtains with the BP probe.

The following graphs show the spectrum variation with different beta source and numbers of polycarbonate layers.

Since we used a plastic scintillator, only the Compton valley is present in the spectrum; the photoelectric peak is completely absent. Moreover, the contribution from the low energy particles is cut off, from the signal threshold set in the electronic acquisition board.

The graph reported in Figure 31 shows the energetic spectrum of the $^{90}$Sr that is compatible with theoretical consideration about energy spectra:

- All the curve shows the same maximum energy
- The spectra areas decrease with the number of polycarbonate layers

Adding more PC layers means to attenuated a bigger number of beta particles, the low value of energy is the same. The attenuation phenomenon only decreases the number of events, not the maximum energy of the particles.

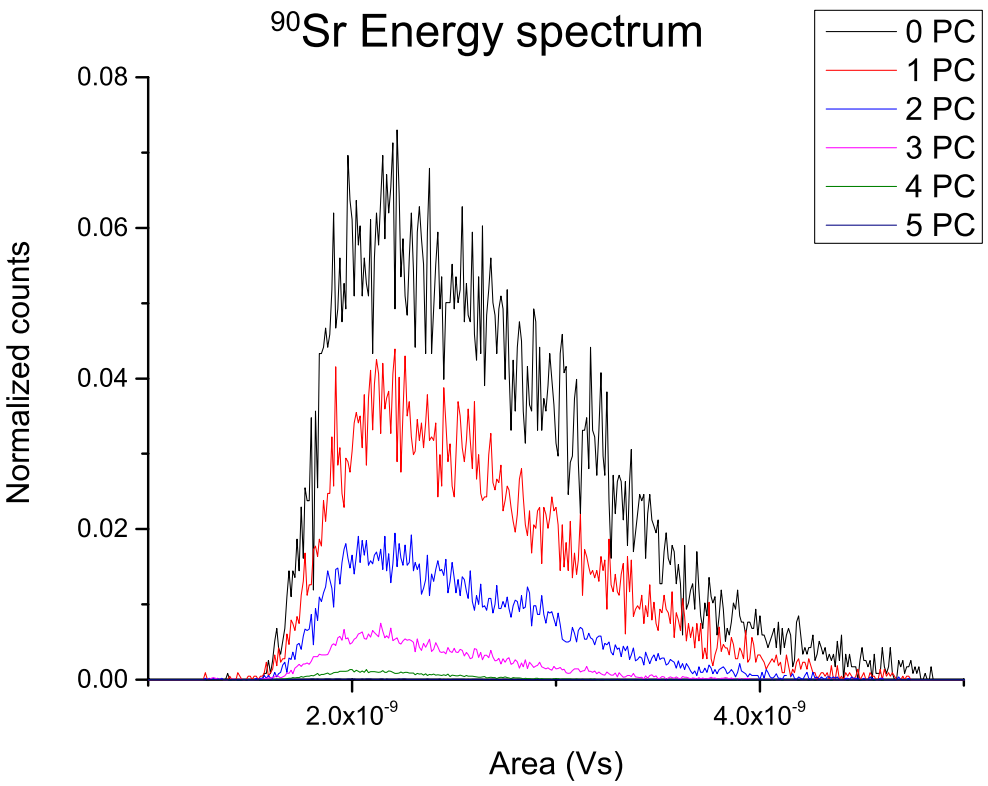


Figure 31: BP Experimental $^{90}$Sr spectra with different number of attenuation layers (1 PC =1.5 mm).

As we already show, the $^{18}$F-FDG behavior is similar to $^{137}$Cs: only one PC layer is enough to remove the beta signal and after it only the gamma signal remains. In fact, the gamma rays are not absorbed by the polycarbonate layers, so with two or three layers the number of counts does not vary, as evident from Figure 32, where the spectra with 1 and 2 PC are overlapping.

The $^{90}$Sr energy spectrum appears less continue than the $^{18}$F-FDG spectrum (Figure 32), due to the different activities of the two sources (the first one is much lower than the second one).

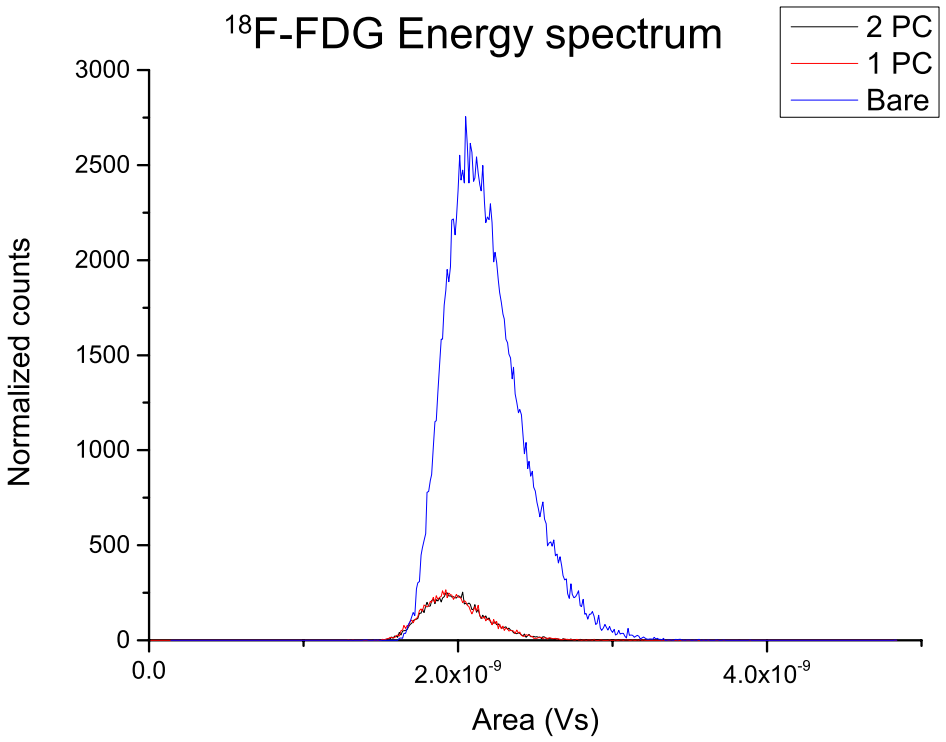


Figure 32: BP Experimental $^{18}$F-FDG paper filter spectra with different attenuation layers (1 PC=1.5 mm).

The lab-made Beta Probe (BP) developed in this work showed a correct response as a beta and gamma detector for medical applications. The good results obtained with the scintillator coupled with the SiPM suggest that this is a feasible solution for beta detection and spectrometry. Moreover, the PSI DRS4 board was tested and proved to be the ideal solution to create the compact beta probe for the final prototype solution instead of using the bulky oscilloscope.

The energy spectrum is very important in nuclear detection, because it give us the possibility to clearly understand many aspects of the observed phenomena: for example, after an appropriate energy calibration, it is possible to define which radioactive source is involved and its level of intensity.

The energy spectrometric information is fundamental in the imaging of a damaged myocardium with the intravascular probe [36], which is capable to map the differential tissue uptake of a beta emitter radiotracer. Different myocardial damaged areas are, in fact, characterized by different level of absorbed $^{18}$F-labelled Matrix Metallo Proteinases; to define a myocardial map, a probe with a differential reading output is then required.

Furthermore, by using the BP it is possible to collect gamma radiation signals, allowing to extract even more information from the data.

The SiPM, coupled with scintillator, is a perfect solution to build a scintillation detector for future endovascular and intra-myocardial probe for an integrated theranostic system utilizing molecularly-targeted radiotracers to deliver localized intra-myocardial therapies. The goal in this case will be the creation of a steerable endovascular catheter-based device that identifies injured myocardium via endocardial detection of systemically delivered beta-emitting radiotracers, and utilizes the molecular signal to guide delivery of therapeutics to the injured tissue via direct intra-myocardial injection [36].

# 5 Development of a luminescence reader based on LED and SiPM

*"... the Motion introduc'd into the Stone did generate the Light upon the account of its producing Heat there, I held it near the* ***Flame of a Candle****, till it was qualify'd to* ***ſhine*** *pretty well in the Dark..."*

*Fellow of the ROYAL SOCIETY, about a Diamond that Shines in the Dark – 1664*

*ROBERT BOYLE*

One of the most frequently used dosimetric techniques is based on passive luminescence dosimeters. Luminescent materials trap electrons in defects of their crystalline structure during exposure to ionizing radiation. When they are appropriately stimulated, electrons are released from the traps, emitting light (luminescence) proportionally to the exposure. Electrons can be released using heat or light, in thermoluminescence dosimetry (TLD) or optically-stimulated luminescence (OSL) dosimetry, respectively.

The most widespread dosimeters are TLDs, but OSL dosimeters have begun to replace them. In fact, OSL presents many advantages: absence of thermal quenching, possibility of multiple readings of the same sample, higher sensitivity and accuracy, greater control of the stimulation power which guarantees higher reproducibility and faster sample reading. The major challenge of the OSL technique is separating the stimulation light from the emission light, which requires complex and expensive optical filtration [92].

Luminescent materials are used in many fields, like personal, spatial and clinical dosimetry, and also in geological, archaeological dating and in the field of national security [43].

Another type of luminescence used for dosimetric purposes is radio-photoluminescence (RPL). The main difference with the previous techniques is that in RPL materials, mainly glass detector (RPLGD), the luminescence centers are not erased by the stimulation [93]. Conversely, the luminescence centers in TLD/OSL disappear after the reading process.

A luminescence reader is mainly built around two components: a light stimulation module and a light detection module. The detection module in a typical commercial reader, the Risø Reader, and in many research readers, is based on a PMT. The innovative solution proposed in this work is a compact modular device based on a LED system as stimulation module and on a SiPM as a light photodetector, both equipped with optical filters.

## 5.1 State of Art for OSL Reader

The reference reader for luminescence is the Risø Reader of Nutech DTU (Figure 33), the reader is a bench-top instrument first developed as a TL reader and subsequently modified to perform OSL as well. The reader was designed for the most commonly used natural (quartz, feldspars) and artificial materials (BeO, $Al_2O_3$:C, $CaSO_4$); therefore, it was equipped with only two stimulation wavelengths, blue and infrared. Recently, it has been equipped with an optional device (Automated DASH for the Risø TL / OSL Reader, 2017), allowing the study of other materials thanks to a new set of filters and an extra green stimulation light.

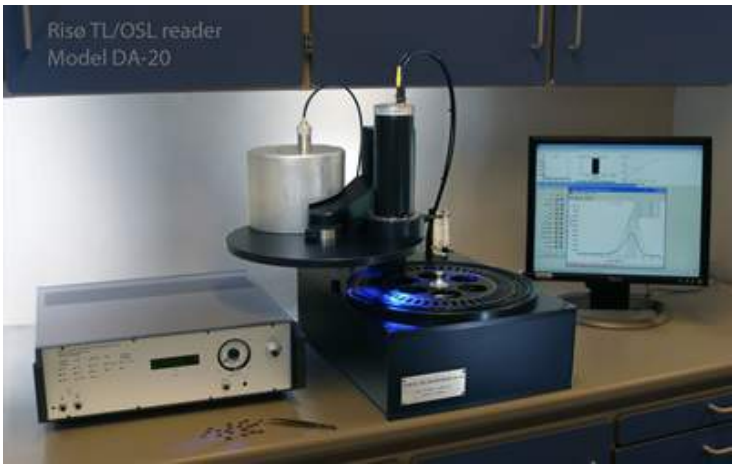


Figure 33: Risø Reader of the Nutech DTU.

Another commercially available reader is the Freiberg Instruments Lexsyg (Figure 34) [94]; this allows greater flexibility of stimulation as it offers a wider range of stimulation light wavelengths and optical filters compared to the Risø Reader.


Figure 34: Freiberg Instruments Lexsyg research.

Both readers are benchtop instruments capable of reading TL, OSL, and photo-luminescent (PL) materials. The readers are equipped with irradiation sources and have sample holders for sequential reading of a large number of samples. Inevitably, in order to offer all these characteristics, the readers are large and expensive.

Other OSL readers have been developed in recent decades [44] , [45], [46]: they are all equipped with photomultiplier tubes, as shown in the following pictures (Figure 35, Figure 36, Figure 37).

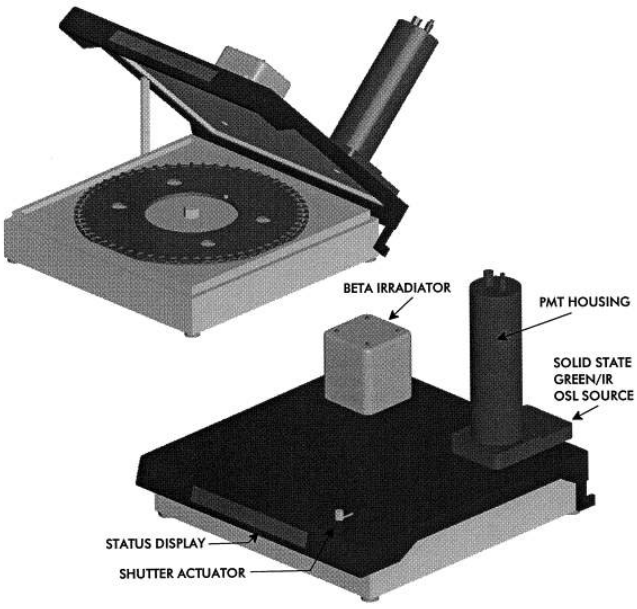


Figure 35: Bortolot OSL reader [44].

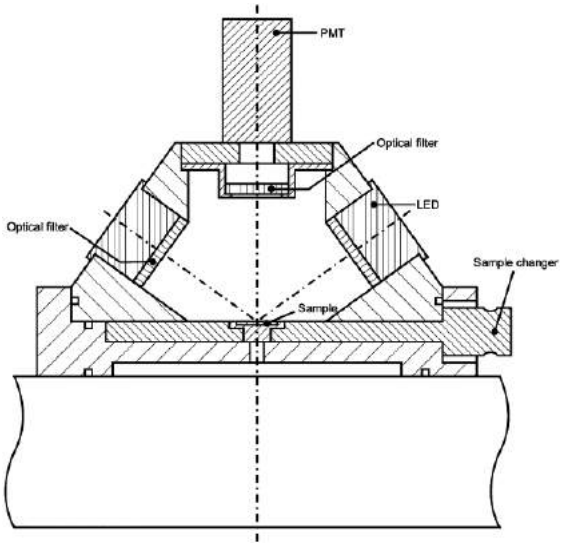


Figure 36: Smetana OSL reader [46].

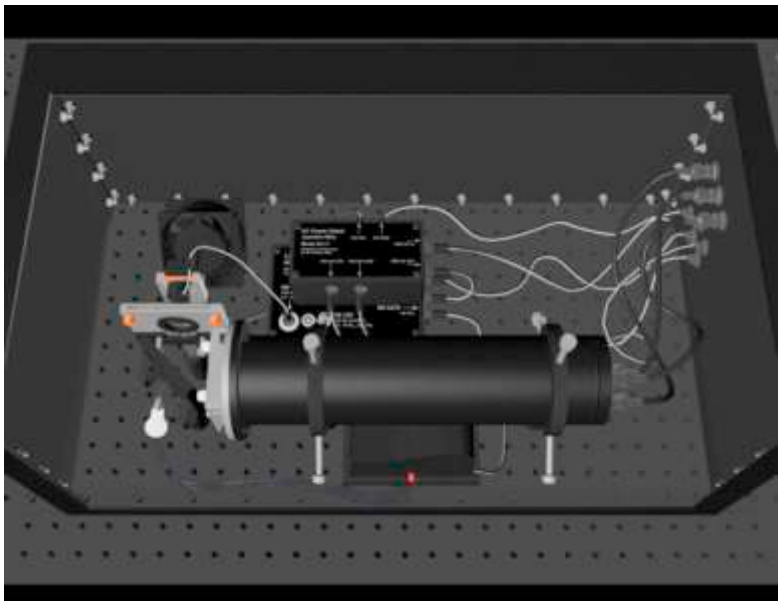

Figure 37: Kearfott OSL reader [45].

However, all these devices are bench-top instruments, and they are not easily portable. Moreover, the mounted PMTs are fragile, sensitive to magnetic fields, large and with the need of high voltage (kV) supply. In order to create a compact and robust luminescence reader a SiPM is used instead of a PMT, providing all the positive features described in the previous chapters. For example, the cost of the reader will be minimized, so that it will be affordable for a greater number of research centers, it is also plausible to develop a reader powered by USB or battery, thus being entirely portable for measurements in the field.

Moreover, all the previous commercial readers are optimized for the stimulation and emission wavelengths encountered with the most commonly used luminescence materials. These readers are not always suitable for measurements with new luminescent materials, which require different stimulation and emission spectra.

## 5.2 Luminescence reader based on SiPM

In our approach (Figure 38), a SiPM based luminescence reader is proposed. The reader is equipped with an LED driving circuit able to delivery light of different wavelengths (between UV and visible), merely changing the LED source. The light emitted is collected by a silicon photo-multiplier (SiPM) equipped with an optical filtering module. The output of the SiPM is acquired and processed by a control and analysis electronic module. A suitable 3D printed holder for the samples was designed.

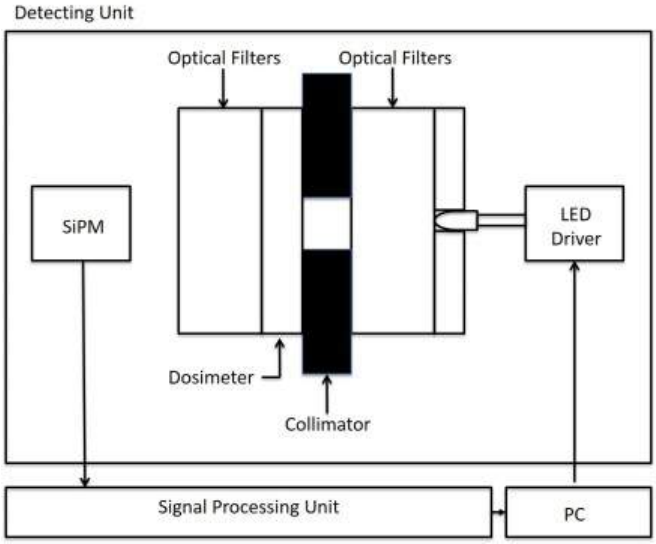


Figure 38: New luminescence reader structure proposed in this work.

This completely modular configuration allows the study of several different luminescent materials: by selecting suitable LED wavelengths and optical filtering modules it is possible to study specific dosimetric materials. A first set-up (Figure 39), based on LED as stimulation module and the SiPM as detection module, was built in order to verify the feasibility of the proposed reader.

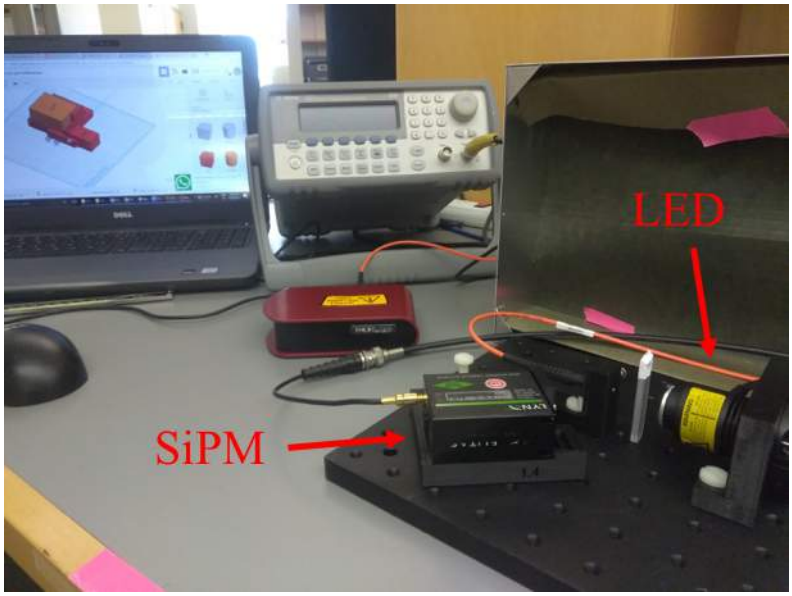


Figure 39: First measurement set-up of the new luminescence prototype reader.

### 5.2.1 SiPM luminescence reader

Two additional setups were then developed and examined: the first prototype works only in continuous wave (CW) mode, while the second one works both in CW and pulsed wave (PW) mode. In CW mode, light stimulation and collection are performed at the same time. In PW mode, the LED light is pulsed, and the light emitted from the sample is collected when the LED light is off.

**Initial set-up**

This setup was built around a cubic sample holder (mod. C4W, Thorlabs), as shown in Figure 41. Inside the cube, a 3D printed piece was inserted to hold the sample, the stimulation and collecting optics. The chosen LED (mod. M375L3 Thorlabs, see LED Figure 40) is driven by a Thorlabs LED (mod. LED01, Thorlabs) driver operated in CW mode.

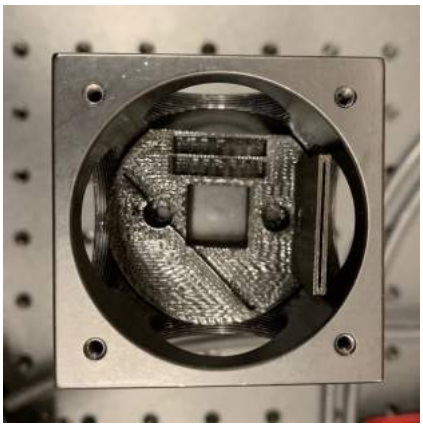

Figure 41: Thorlabs cage cube with a 3D printed base holder for the sample.

Figure 40: M375L3 LED from Thorlabs.

The photoluminescence from the samples was analyzed by two devices: a compact spectrophotometer from Thorlabs, mod. CCS200 (Figure 44), and a Silicon Photo Multiplier from Excelitas, model LynX, part number NR-A-33-050-T1-A (Figure 42 and Figure 43). The first device (Figure 45) was used to record the samples emitted spectra, while the latter was used to transduce the emission signal in terms of mean voltage. In both cases, the light was guided from the sample to the devices by using an optical fiber.

| **Detector** | | | | | |
|---|---|---|---|---|---|
| **Parameter** | **Condition** | **Min.** | **Typ.** | **Max.** | **Unit** |
| Effective Active Area | | | 3 x 3 | | mm |
| Num. Of Microcells | | | 3600 | | |
| Microcell Size | | | 50 x 50 | | µm |
| Spectral Bandwidth | | 350 | | 950 | nm |
| Peak Wavelength | | | 500 | | nm |
| **Module** | | | | | |
| **Parameter** | **Condition** | **Min.** | **Typ.** | **Max.** | **Unit** |
| Positive Supply Voltage | | 4.5 | 5.0 | 5.5 | V |
| Positive Supply Current | | | 350 | 1000 | mA |
| Power Up Settling Time | | | 15 | | s |
| Output Voltage Swing | High impedance | | | +5 | V |
| Responsivity | @525 nm in 50 Ohm | | 0.75 | | V/nW |
| Bandwidth | | 1 | 1.5 | | MHz |
| NEP | | | 1.0 | | $fW/(Hz)^{1/2}$ |
| Output offset voltage | | | 1.5 | | mV |
| Storage Temperature | | -10 | | +50 | °C |
| Operating Temperature | | +5 | | +50 | °C |

Figure 42: SiPM Lynx Excelitas mod. NR-A-33-050-T1-A datasheet.


Figure 43: The SiPM LynX, mod. NR-A-33-050-T1-A from Excelitas.

| Item # | CCS100 | CCS175 | CCS200 |
|---|---|---|---|
| Wavelength Range | 350 - 700 nm[a] | 500 - 1000 nm | 200 - 1000 nm[a,b] |
| FWHM Spectral Accuracy | <0.5 nm @ 435 nm | <0.6 nm @ 633 nm | <2 nm @ 633 nm |
| S/N Ratio | ≤2000:1 | | |
| CCD Sensitivity | 160 V / (lx · s) | | |
| Integration Time | 10 µs - 60 s | | |

Figure 44: CCS200 Thorlabs compact spectrometer specification.

Figure 45: The CCS200 spectrometer from Thorlabs.

The first measurements were made in order to characterize the spectral shape of the light source in a CW mode. The LED beam was acquired with a beam splitter that reflected approximately 10% of the LED light beam into the optical fiber that was coupled to the Thorlabs spectrophotometer and then the spectrum was recorded. This procedure was repeated with different optical average power (20 mW, 80 mW and 140 mW). The acquired spectra shown in Figure 46 reveals the spectral shape of the light source used to stimulate the samples.

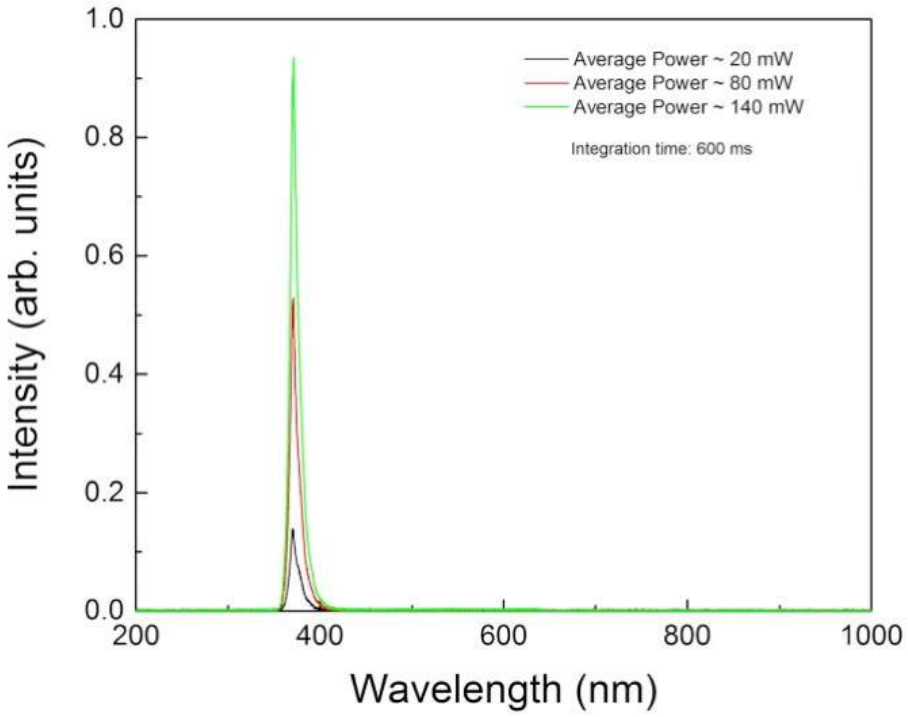


Figure 46: The spectra of the LED at different average optical powers.

**Second set-up**

A second prototype was created to collect the signal still using the PW mode of the UV-LED source. The electronic board to control the LED was developed in the laboratory, as shown in the rendering in Figure 47 and Figure 48. The mechanical structure of this prototype was created using a 3D printer (Figure 49).

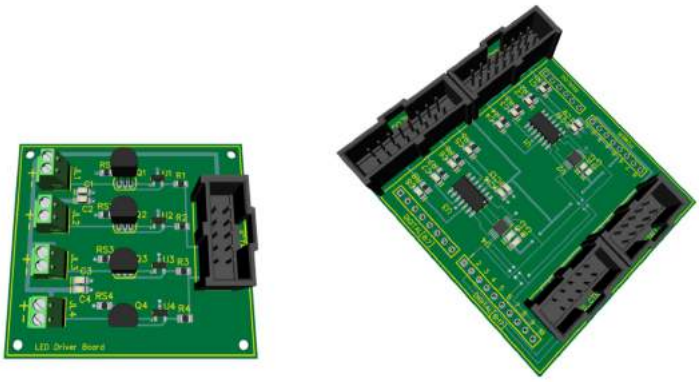

Figure 47: 3D rendering of the LED driver board (left) and of the main control board (right).

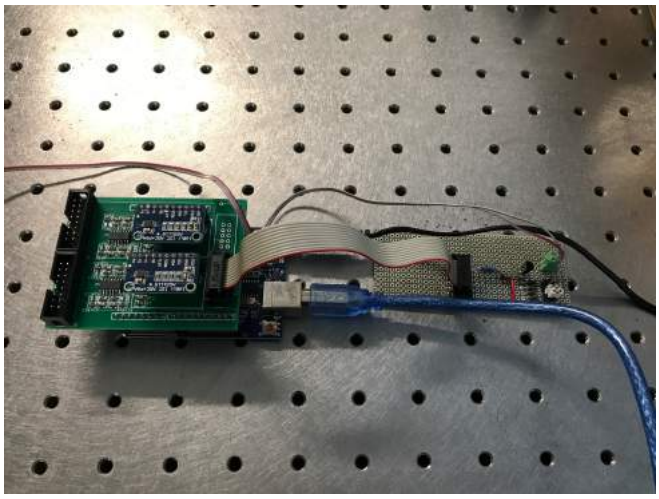

Figure 48: LED driver used for the luminescence reader.

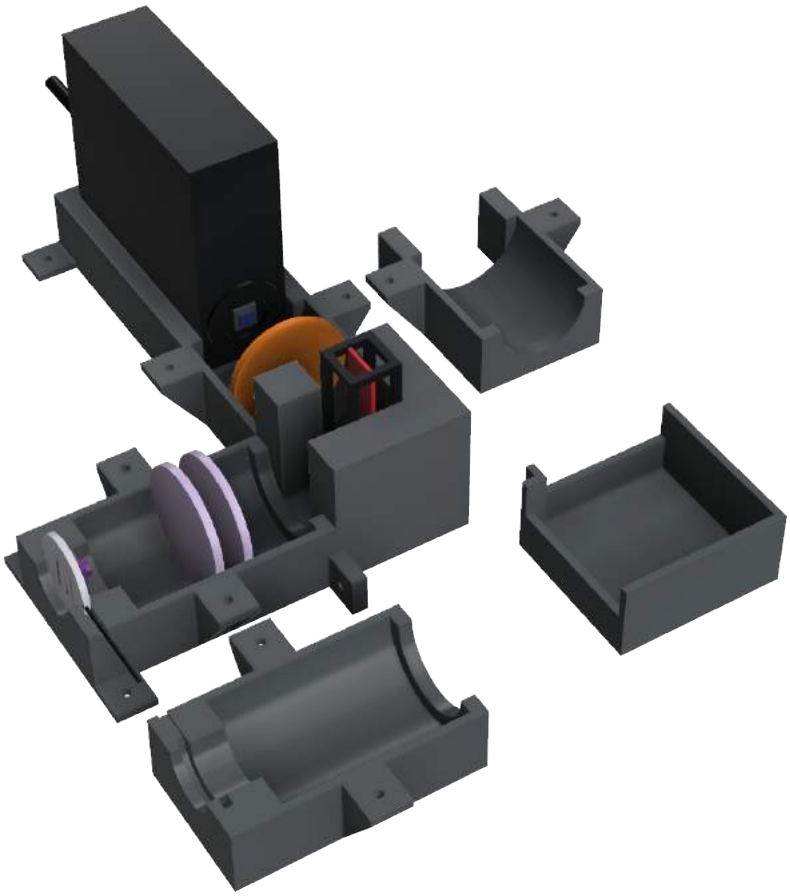

Figure 49: 3D printed support for the luminescence measurements. From the left the LED, the optical filter holder, the sample and the SiPM holder.

Since LEDs are current polarized devices, the light output intensity is linear with the current itself (at least for low current values). Therefore, a constant current LED driver circuit is required to drive the LEDs in a stable manner. The circuit is based on a trans-conductance amplifier, which is a voltage to current converter; it allows to drive the LEDs in both CW and PW mode. The control signals for the LED driver circuit are generated by a suitable microcontroller unit (MCU) as shown in Figure 50.

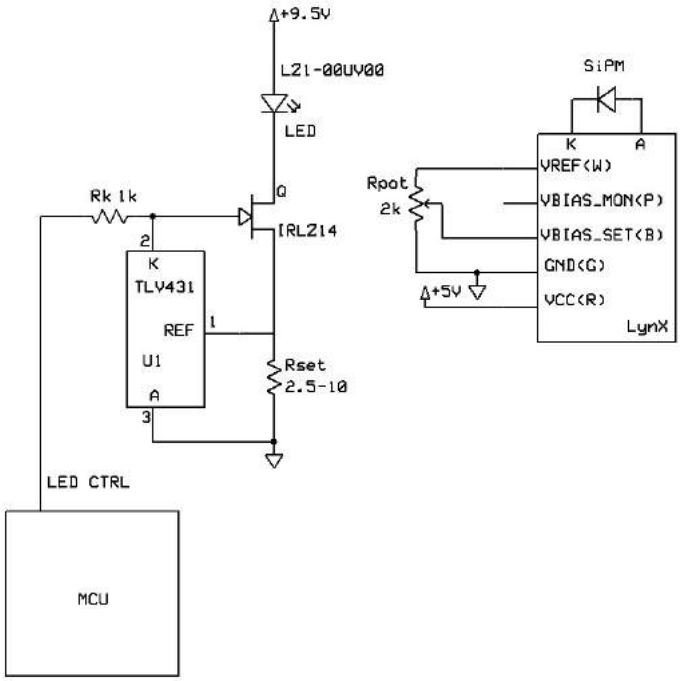


Figure 50: The readout system for RPL is composed by the stimulation part (MCU, LED driver and UV LED) and the detection part (SiPM, LynX Module and Lynx Module control network).

When the LED driver is operated in CW mode, the “LED CTRL” signal is always held at +5V (TTL logic level) during the stimulation and collection of the light signal. If the LED driver is operated in PW mode the “LED CTRL” signal is switched ON and OFF with a frequency of 250 Hz (period 4 ms) and a duty cycle between 0.25% (ON time 10 μs) and 2.5% (ON time 100 μs).

The LED driver is based on a bandgap voltage reference (TLV431, Texas Instruments) with nominal voltage output of +1.24 V, and a logic level N-channel MOSFET (IRLZ14). When the “LED CTRL” signal is ON, small current flows through Rk, allowing the bandgap voltage reference to hold the “REF” pin at a voltage par to +1.24 V. The current flowing through Rset, whose value is settable between 2.5 and 10 Ω, is then +1.24 V/Rset (Iref is then settable between 124 mA and 496 mA). The current through Rset is the same current flowing through the MOSFET (drain to source) and the

LED. If the current becomes too high, then the K pin of the voltage reference (or the gate voltage of the MOSFET) is decreased in order to hold the REF pin at +1.24 V; if the current becomes too low, the gate voltage is, instead, increased. The described negative feedback allows to keep the current through the LED constant, also when the +9.5 V power supply is not well regulated. Therefore, the circuit is configured as a constant current sink.

The Lynx SiPM module is controlled with a resistive control network (Rpot). When the module is powered up (i.e. VCC pin is at +5V and GND pin is at 0V), the Vref pin is regulated to +4.525 V. A fraction of this voltage is fed back to the Vbias_set pin in order to the set the voltage bias of the SiPM through an internal network. If required the bias voltage of the SiPM can be monitored by measuring the Vbias_mon pin voltage using a voltmeter.

The output of the LynX module is connected to a data acquisition board (DAQ). The LynX is just a pre-amplification and conditioning stage of the SiPM detector, which is biased up to 100V by an internal network.

In order to perform a CW stimulation and acquisition, the “LED CTRL” pin must be held HIGH; therefore, the LED is working in constant current mode. Then, the mean value of the voltage measured by the data acquisition system can be acquired.

To perform a PW stimulation and acquisition, the “LED CTRL” pin is square pulsed between LOW and HIGH with a ON period between 10 µs and 100 µs and a frequency of 250 Hz. The square pulse signal is used both to drive the LED and as an external trigger for the data acquisition system. The output from the LynX is then averaged 128 times before being acquired to reduce noise.

In order to decrease the rise time and fall time of the LED driving system a new architecture was developed. The high-speed LED driver circuit is based on a MCP1407 MOSFET driver (Microchip), featuring a 6 A peak current (Figure 51).

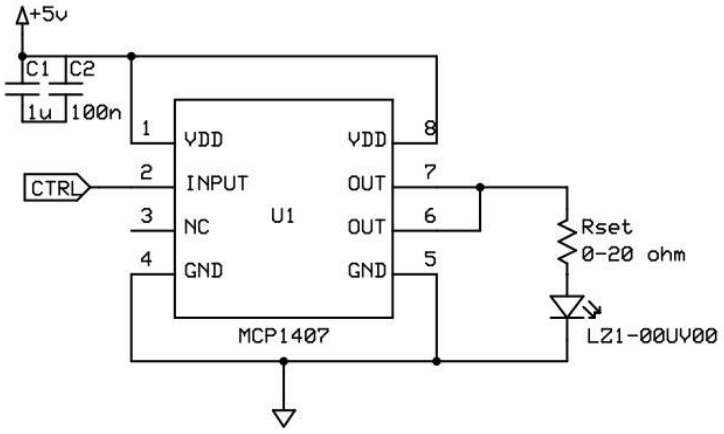


Figure 51: Architecture of the LED driving system used to achieve a rise and fall time of a few hundreds of ns.

In the previous circuit (Figure 50), which was based on a TLV431 constant current sink, the response speed was limited by the rise and fall time of the current regulator (few μs). Moreover, it was hard to switch high currents (more than a few hundred mA) because of the capacitive loads of the FET, wires and LED itself: the TLV431 is, in fact, not stable when driving large capacitances, resulting in unwanted oscillations when switching high currents. The proposed circuit does not include a current regulation circuit, and the current through the LED is limited by the sum of the output impedance of the MCP1407 and the Rset resistor value. The integrated circuit is driven by a TTL logic signal generated by a microcontroller (CTRL port on pin 2).

The output of the MCP1407 (OUT, pin 6 and 7) is directly connected to the anode of the LED through a Rset resistor. When supplied by a regulated 5V power supply (pin 1 and 8), the OUT pins are able to drive to 5V a capacitive load in the order of 10 nF in just a few tens of ns. The current required is supplied by the decoupling capacitors C1 and C2. When the CTRL input is LOW, the output pins are grounded and no current flows through the LED; when the CTRL input is HIGH, the output pins are at VDD (5V) and the current through the LED is calculated as follows: the voltage drop across the LED is given by the difference between VDD and the product between the LED current itself and the sum of the output impedance of the MCP1407 and the Rset resistor. Therefore, by measuring the voltage drop across the LED, the current is obtained from the I-V characteristic of the diode. When the Rset resistor is removed, the current is about 800 mA.

The current can be decreased by increasing the value of the Rset resistor. The response of the circuit (measured by a 2022C Tektronix Scope) is shown in Figure 52.


Figure 52: (A) Shape of a 1 µs pulse generated by a GPIO pin of the microcontroller; (B) Fall time of the TTL signal generated from the microcontroller; (C) Shape of the LED driving signal on the output of the MCP1407 (yellow line) and shape of the light signal detected by the SiPM LynX Module (light blue line).

The rise and fall times of the digital TTL signal from the microcontroller are less than 20 ns, but the GPIO (General Purpose Input-Output) current (limited to 40 mA) is not high enough to directly drive the LED directly, especially at high speed due to stray capacitance. However, thanks to the MCP1407, the rise and fall times of the LED driving signal on the output are less than 100 ns. The response of the SiPM to a 1 µs LED pulse is also shown in the previous figure: the shape of the detected waveform suggests that the 10 MHz cut-off frequency of the LynX module response is a limiting factor too. Therefore, a faster response can only be obtained with a stimulation and detection modules modification.

### 5.2.2 Luminescence material tested

An ongoing research on silver activated phosphate glasses (RPLGD) offered the opportunity to test the innovative luminescence reader and demonstrate its flexibility. The RPLGD dosimeters are glass plates as is visible in Figure 53.

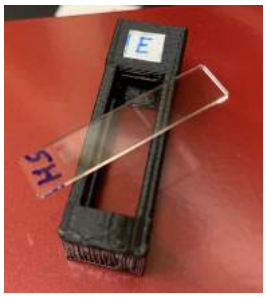

Figure 53: Silver activated phosphate glasses samples.

After irradiation, the RPLGD has some electrons in the traps (color centers), which originates an emission centered approximately at 635 nm, when stimulated (excited) with UVA light (Figure 54). After the excitation process, the electrons return to the color center traps, and for this reason, the samples can be re-read for a single irradiation and this characteristic is suitable for our purpose, because it allows multiple test for the same sample of our reader. Only a thermal annealing around 400 °C, during at least 1:30 hour can erase the color centers of the RPLGD [95].

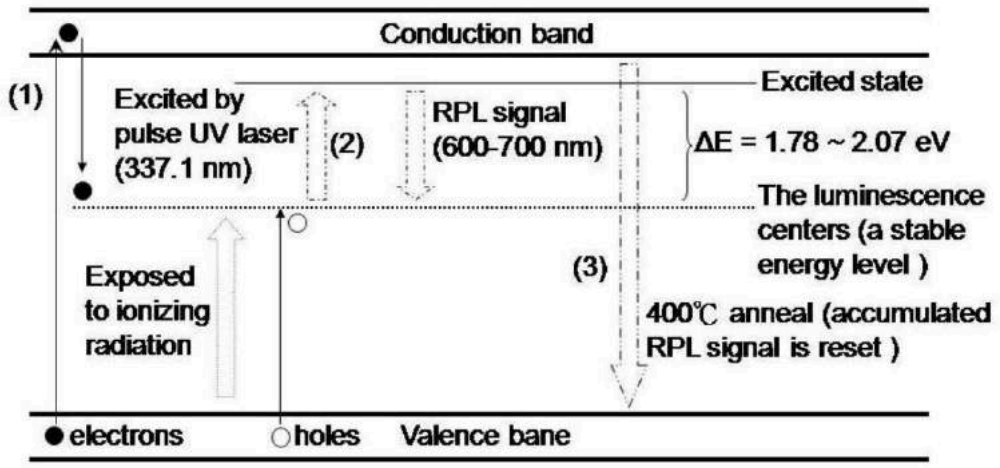


Figure 54: The energy levels of RPLGD [95].

RPLGD samples were irradiated at the linear accelerator Elekta Synergy (Figure 55) at San Lucca Hospital (Lucca, Italy) using 6 MV X-rays, a 600 MU/min dose rate and a 15x15 $cm^2$ irradiation field to deliver the following doses: 0.1 Gy, 0.5 Gy, 1.0 Gy, 5.0 Gy and 10.0 Gy. In Figure 56 it is possible to see the corresponding emitted orange light if UV-light stimulates them.

Figure 55: Linear accelerator Elekta Synergy, Lucca Hospital.

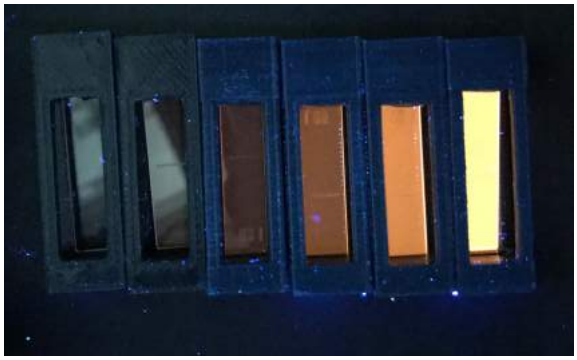

Figure 56: UV-LED stimulated RPLGD sample with different dose. Starting from the left we have the not irradiated sample, that is transparent, and the incremental irradiated samples, that emit in the orange wavelength region, after a dose of 0.1, 0.5, 1, 5, 10 Gy.

As we use RPLGD glass sample, a 3D printed support was made (Figure 57). However, the development is foreseen of other sample holders whose shape will depend on the type of sample to be analyzed.

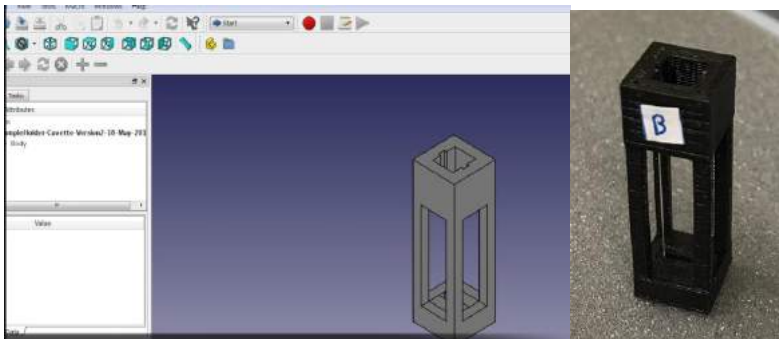


Figure 57: A designed homemade sample holder for the RPLGD dosimeter, the CAD software on the left and the 3D printed holder on the right.

The absorption spectra of the RPLGD were obtained by a UV-VIS spectrophotometer system (Agilent Cary 5000). In this experiment, five samples were used with the following doses: 0.1 Gy, 0.5 Gy, 10 Gy, 30 Gy, 100 Gy, and 500 Gy. Figure 58 shows the recorded spectra, which seem to comprise two overlapping absorbance bands in the spectral region of 300 nm to 500 nm. Within this region, the higher energy band is centered around 310 nm, and the presence of a shoulder around 370 nm, suggests that the lower energy absorbance is centered in that spectral position. This result indicates that the stimulation light must be tuned to one of the two bands, to achieve the highest RPL intensity.

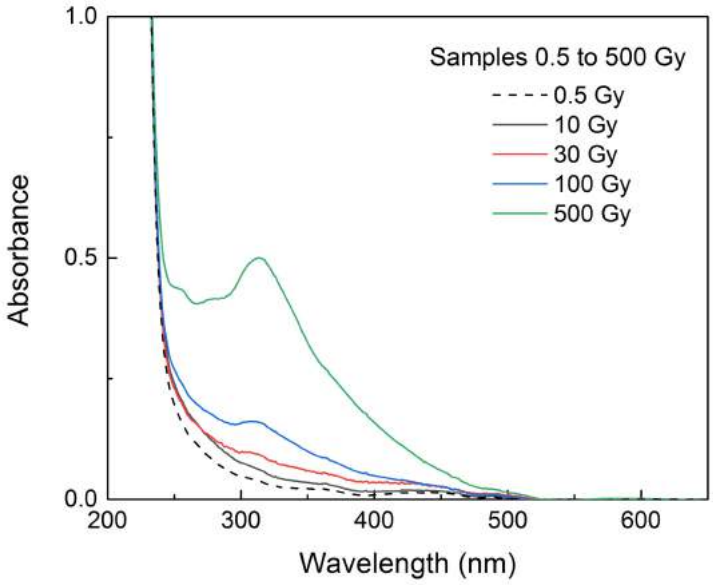


Figure 58: Absorbance spectra of RPLGD samples measured using an Agilent Cary 5000 spectrophotometer.

The RPLGD set-up required optical filtering, all performed with Thorlabs filters: in stimulation the FGUVM (Figure 59) and FGUVM011M (Figure 60) to assure that the stimulation spectrum is only centered at UV wavelengths; in emission, the FELH0450 (Figure 61) and the FELH0600 (Figure 62) to avoid excitation light reaching the detector.

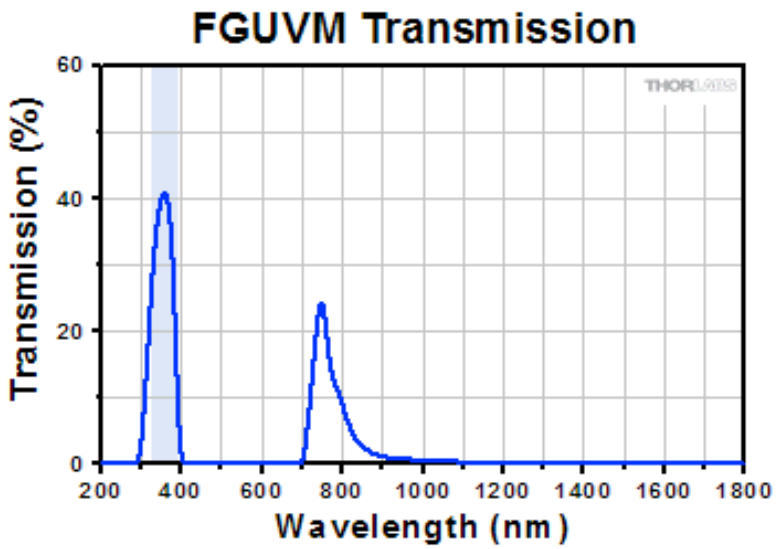


Figure 59: Thorlabs FGUVM transmission.

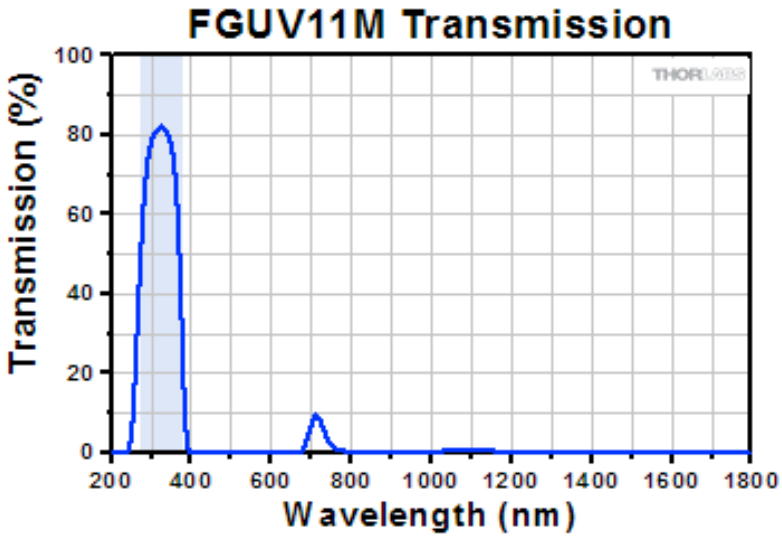


Figure 60: Thorlabs FGUV11M transmission.

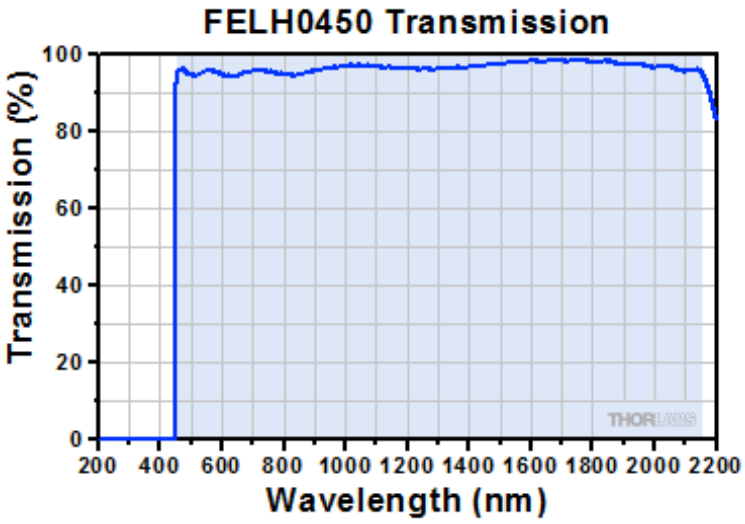


Figure 61: Thorlabs FELH0450 transmission.

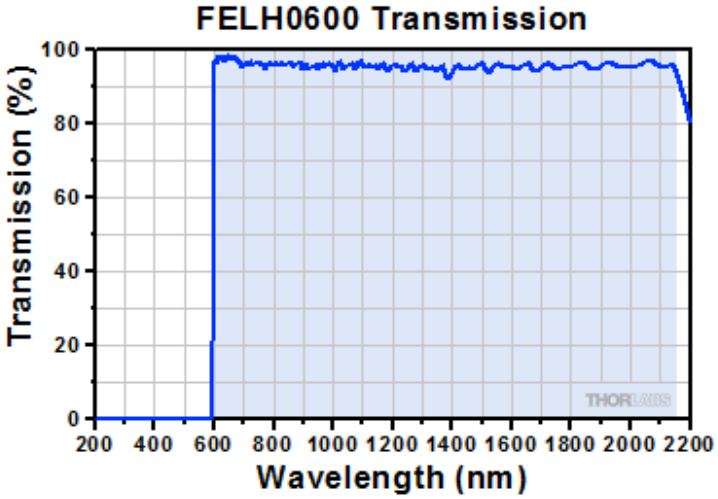


Figure 62: Thorlabs FELH0600 transmission.

The complete scheme of the second RPLGD prototype reader is visible in Figure 63.

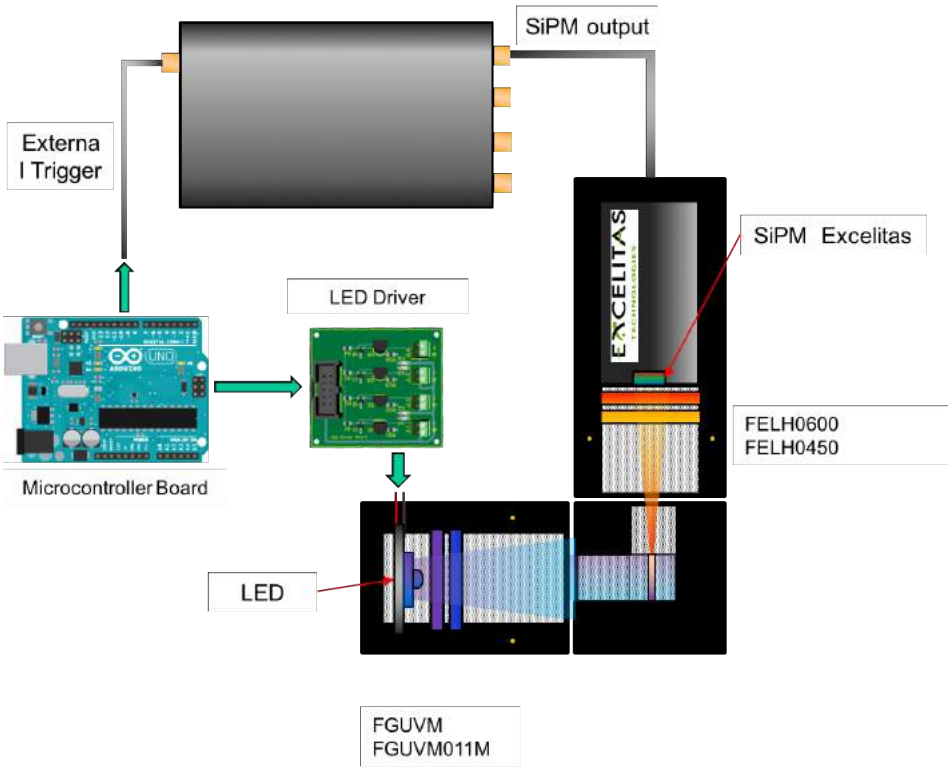


Figure 63: RPLGD reader set-up scheme: on the left side, the stimulation module with the LED and optical filter and on the right the emission part with the SiPM.

With the CW configuration set-up, the samples were stimulated, and the emission of photoluminescence was collected at 90° from the stimulation beam, as shown in Figure 64 for the first prototype and in Figure 65 for the second one.

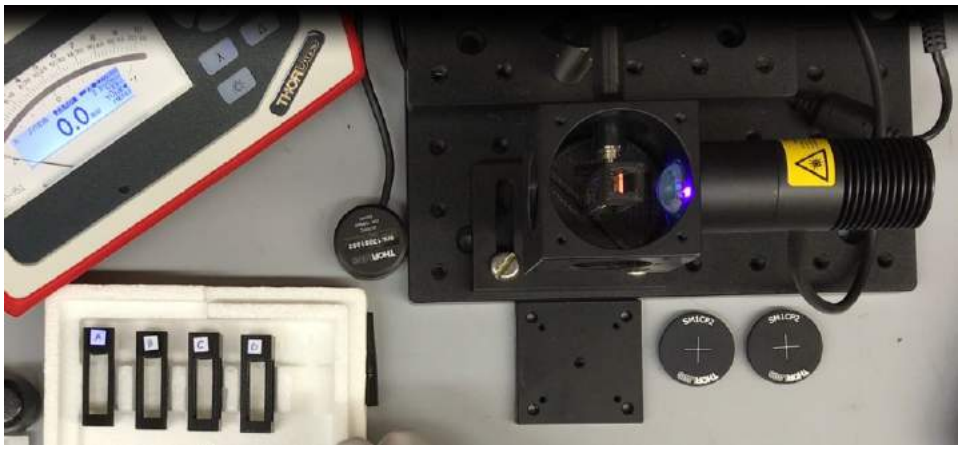

Figure 64: The complete and compact first prototype to acquire the RPL signal from the samples.

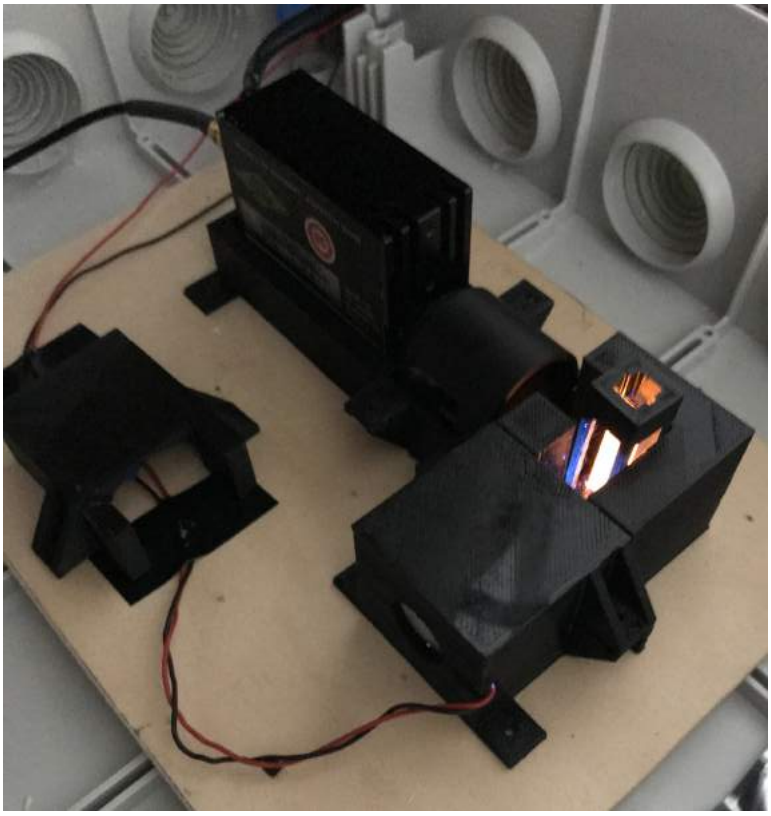

Figure 65: The second prototype used to acquire the RPL signal from the samples using the CW and the PW.

## 5.3 Results and discussion

The emission spectra of the RPLGD samples, acquired with the Thorlabs mod. CCS200 spectrometer were recorded in CW stimulation mode using the first prototype reader, and results are shown in Figure 66. The narrow band centered around 370 nm is the stimulation light, and the broadband centered around 635 nm is the photoluminescence emission of the samples. The glitch observed between approximately 645 and 650 nm is an artifact produced by a detected malfunction of the spectrometer CCS200, reported in the next paragraphs.

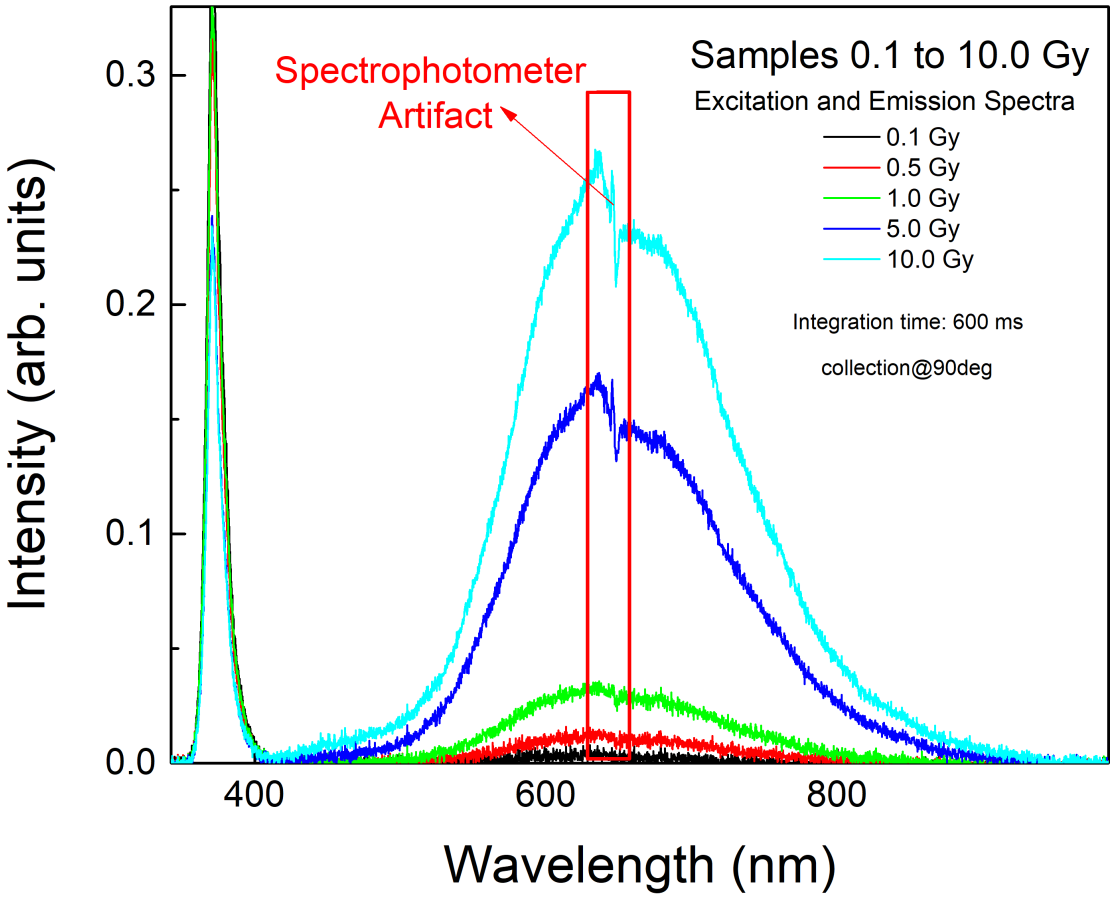


Figure 66: Spectrophotometer artifact in the excitation and emission spectra using Thorlabs CCS200 of five RPLGD samples.

To understand the origin of the previously mentioned artifact (glitch), a conventional LED lamp was used to illuminate the spectrometer CCS200 in two different configurations of light collection: with and without the optical fiber connection. Both

spectra presented the artifact, thus indicating that the malfunction was due to the CCS200 spectrometer and not to the optical fiber, as shown in Figure 67 and Figure 68.

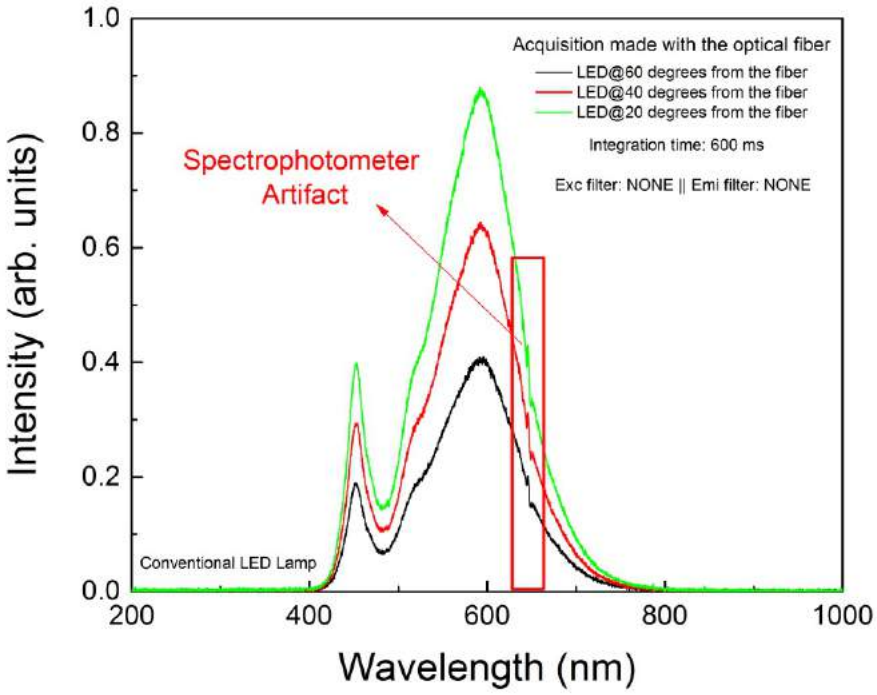


Figure 67: Spectra of a conventional LED lamp, at different angles, with an optical fiber coupled to the CCS200.

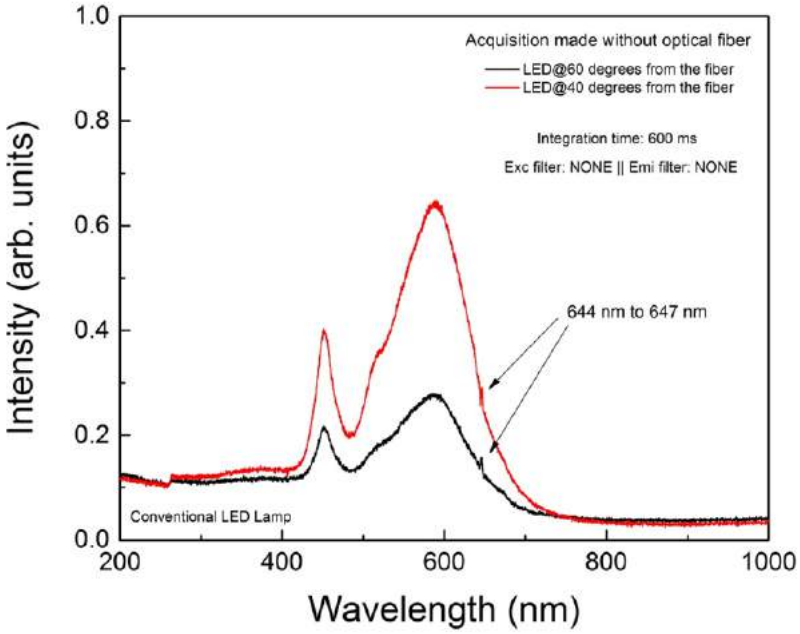


Figure 68: Spectra of a conventional LED lamp, at different angles, without an optical fiber coupled to the CCS200, in order to check the artifact.

The artifact confirmation tests proved that there is no phenomenological behavior of the RPLGD emission associated with the discontinuity centered around 645 nm. The photoluminescence intensity of three wavelengths, before the artifact (620 nm), near the maximum of the emission (636 nm) and after the artifact (690 nm), are shown in Figure 69. Those intensity values were then plotted as a function of the irradiated doses, showing a linear behavior in the considered dose range for all the selected wavelengths, as shown in Figure 70.

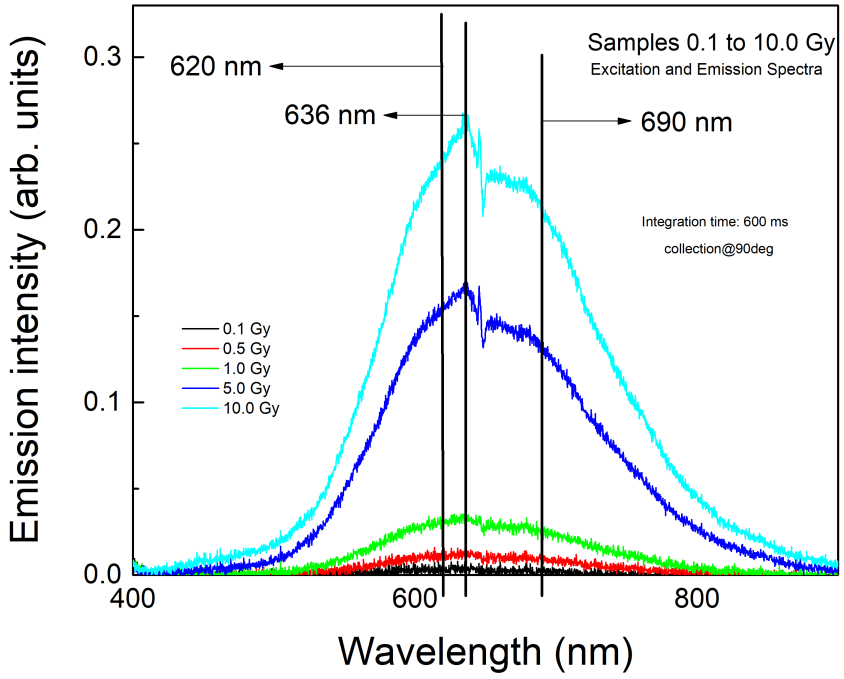


Figure 69: Selection of three wavelengths from the emission spectra to compare the light emission intensity of the different doses.

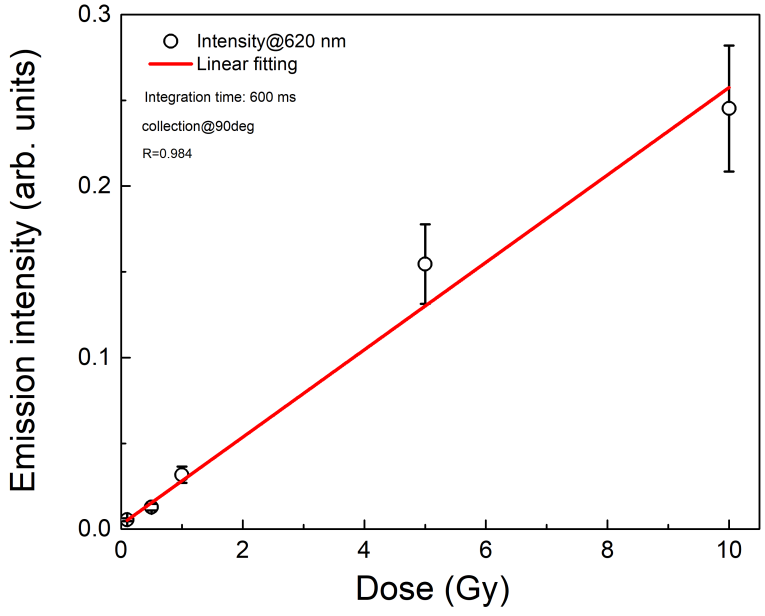


(a)

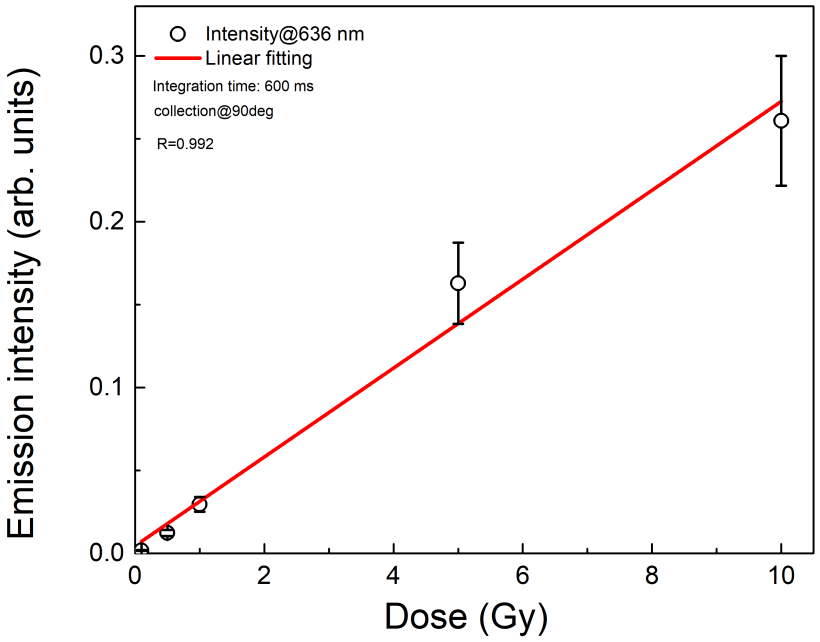


(b)

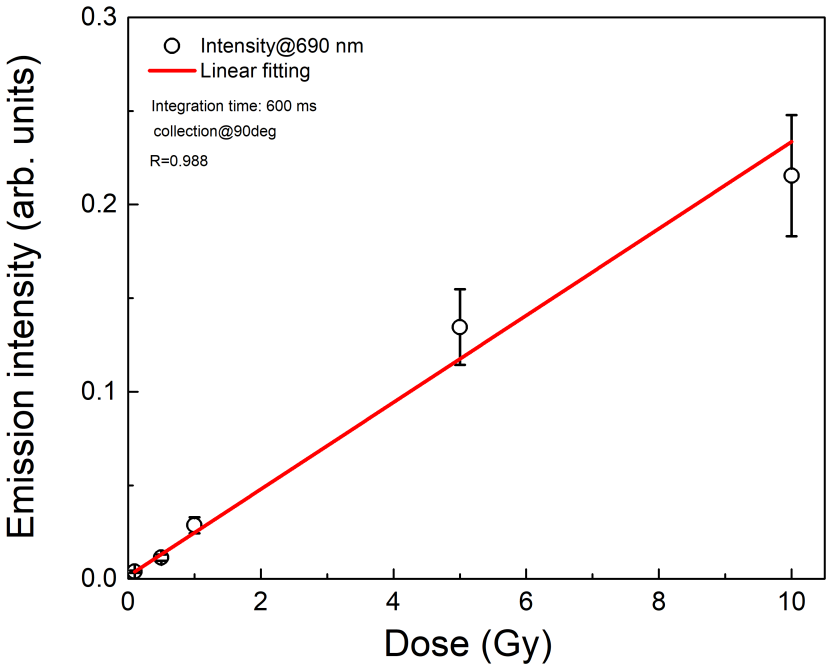


Figure 70: Linear behavior between dose and light emission using CCS200 at 620 nm (a), 636 nm and at 690nm (c).

(c)

As described earlier, our optical system collects the RPL signal simultaneously into a compact spectrometer and a silicon photomultiplier (LYNX). This dual real-time acquisition allows checking that the described and presented linearity of the intensity

emission as the function of the irradiated doses is also detected in the LYNX SiPM, as shown in Figure 71.

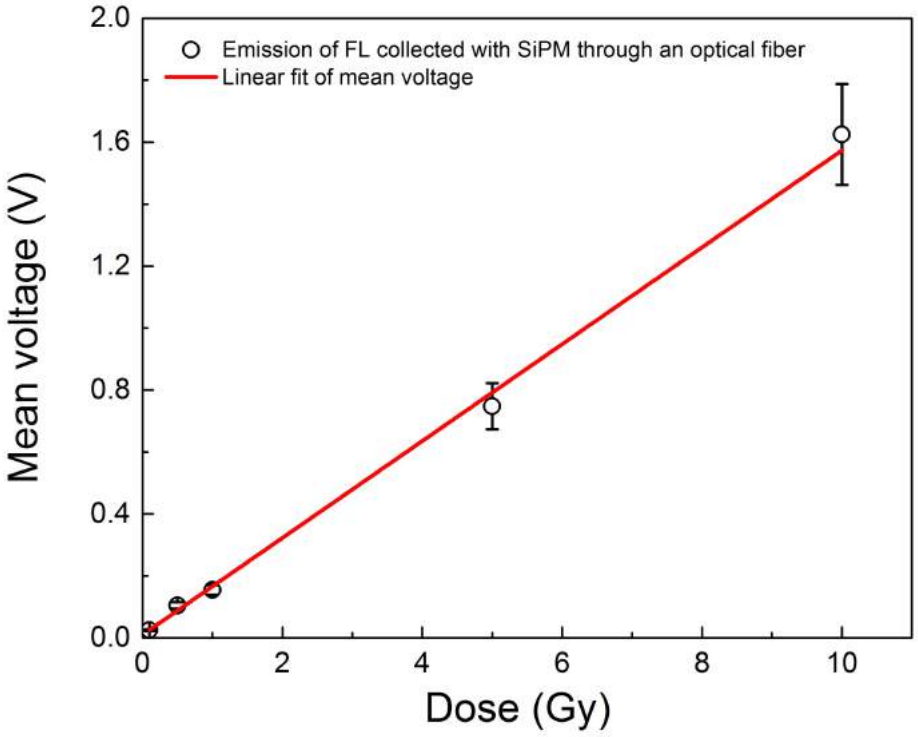


Figure 71: Linear behavior between dose and emission light using LYNX SiPM in CW mode

The same procedure was implemented in the second prototype (optical setup) using the LED in pulsed-wave mode. In this optical setup, an LED driver based on ATMEGA328 was used to measure the lifetime decay of the photoluminescence, by exciting the sample with a periodic function (square wave) and collecting the emitted light, reducing the interference of the stimulation light. In this case, the recorded data was acquired only with the SiPM, while the compact spectrometer was used to check if any scattered stimulated light reaches the SiPM. The average value of the maximum plateau of the square stimulated pulse was used to verify the presence of a linear behavior of the emission signal as a function of the irradiated dose. Figure 72 shows the signal for the not irradiated sample and the sequence from Figure 73 to Figure 77 show the obtained results and analysis made for the pulsed mode of the irradiated samples.

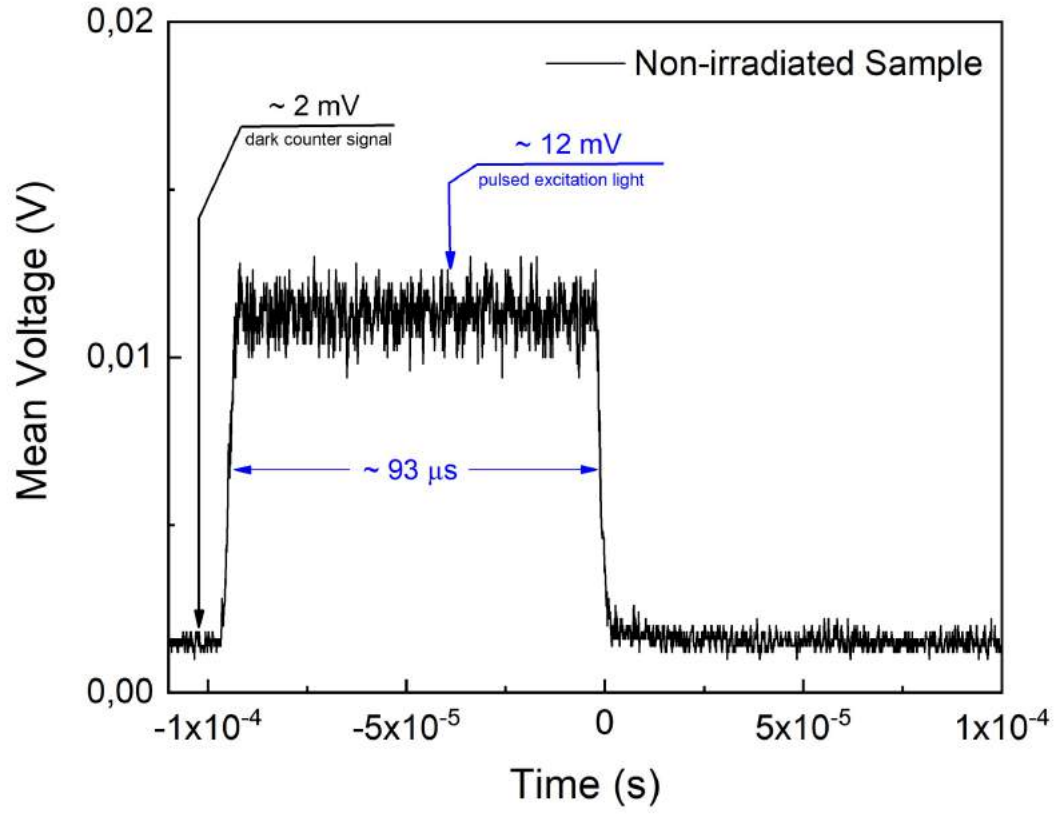


Figure 72: PW measurement of the blank sample not irradiated.

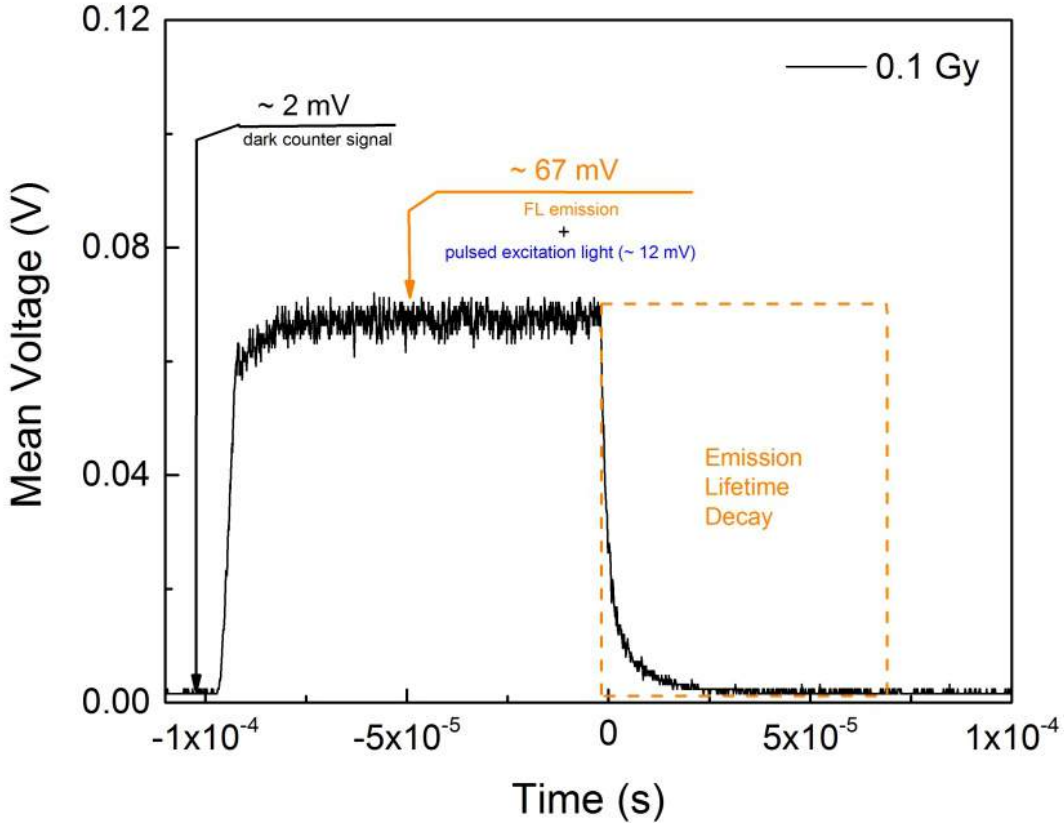


Figure 73: PW measurement of the 0.1 Gy sample.

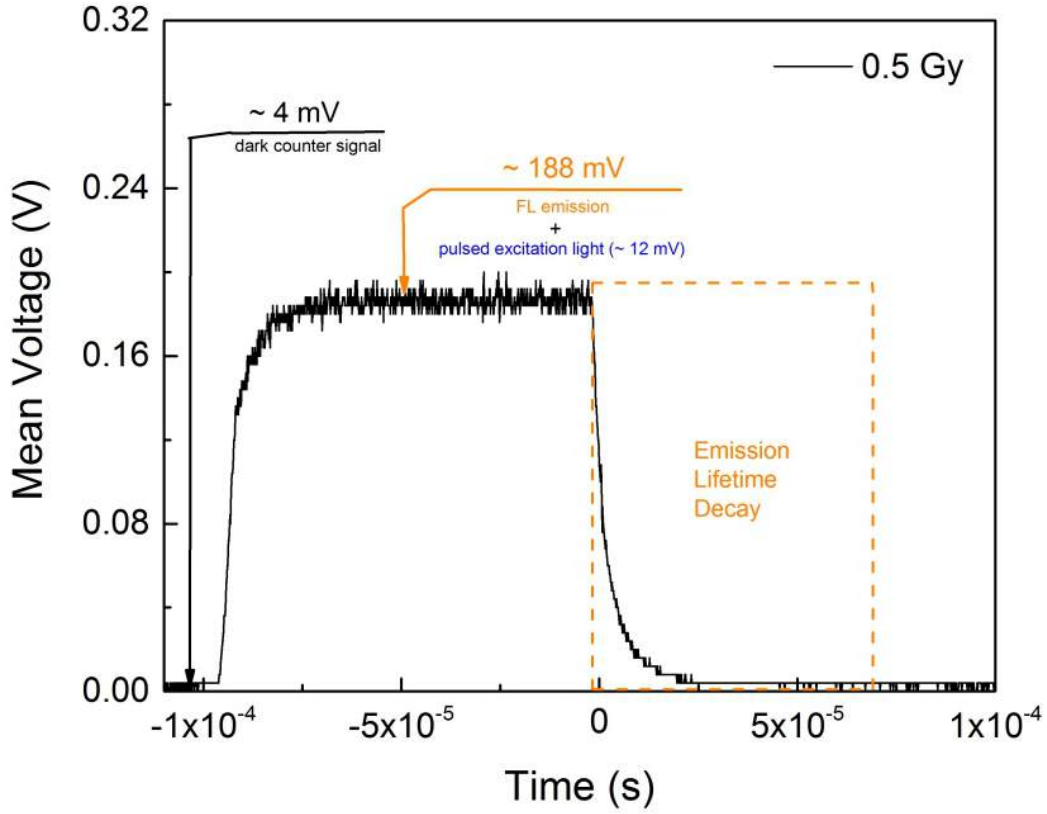


Figure 74: PW measurement of the 0.5 Gy sample.

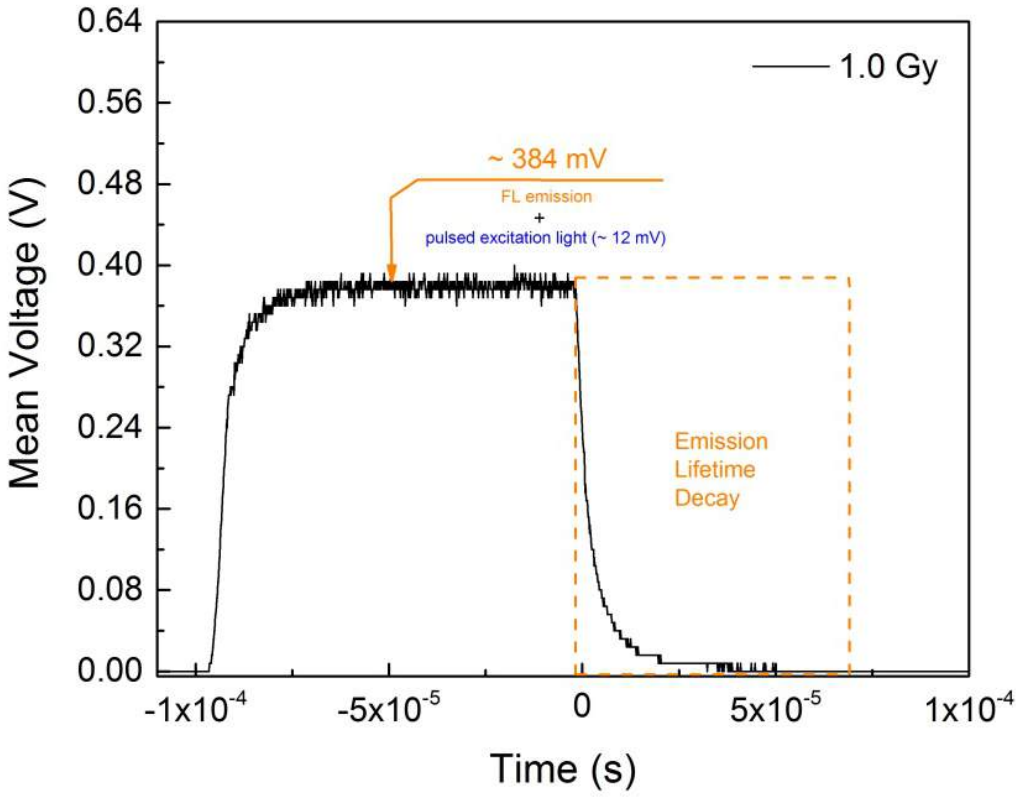


Figure 75: PW measurement of the 1.0 Gy sample.

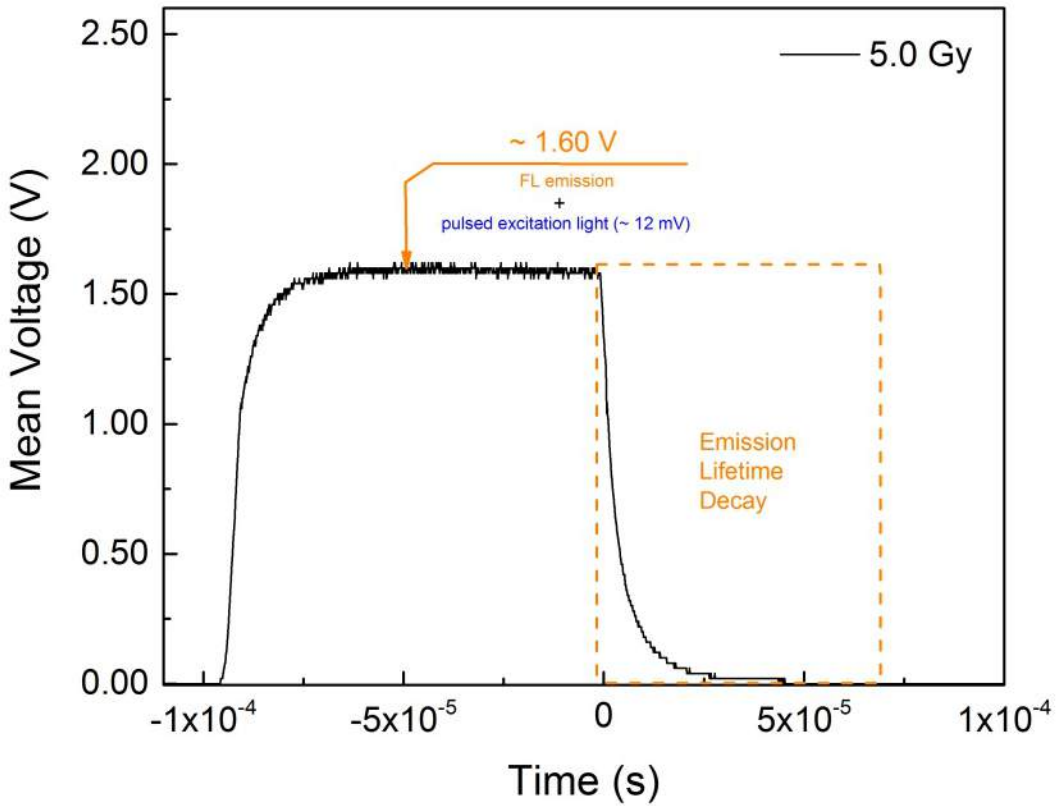


Figure 76: PW measurement of the 5 Gy sample.

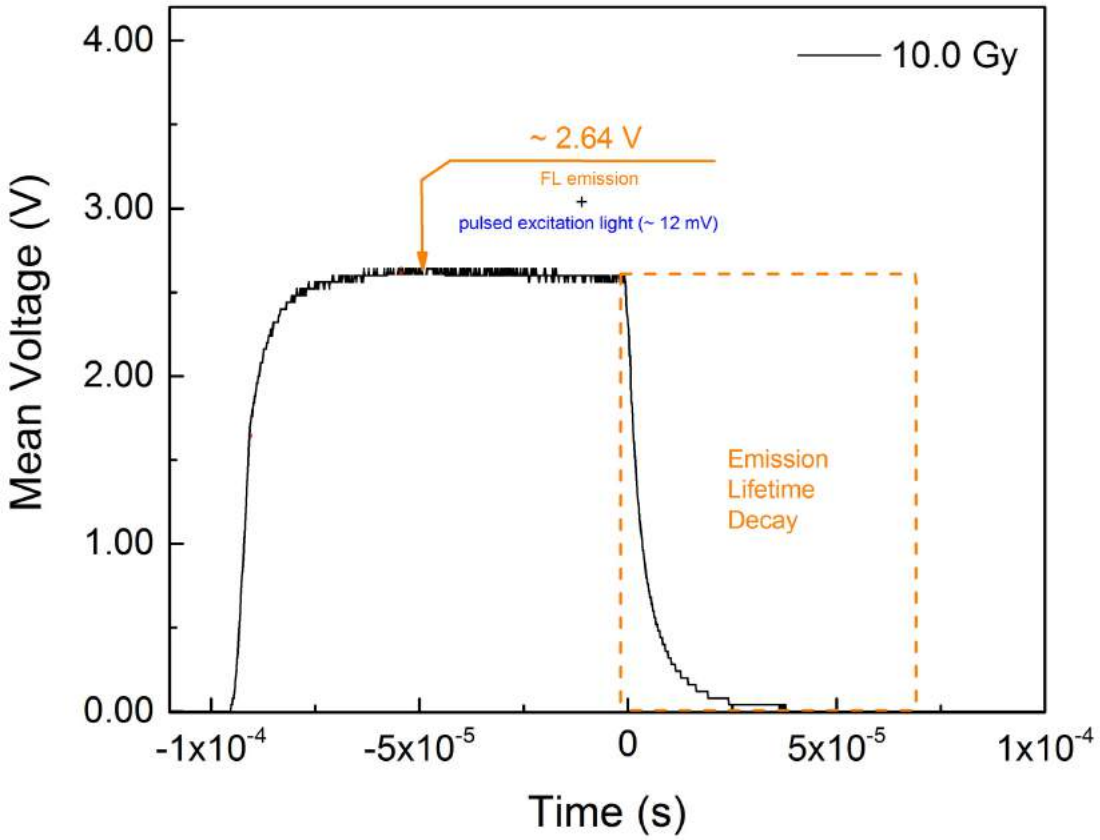


Figure 77: PW measurement of the 10 Gy sample.

The results show the same linear response (Figure 78) as obtained using the previous set-up, except for the highest dose value (10 Gy), which appears to be due to SiPM saturation effects.

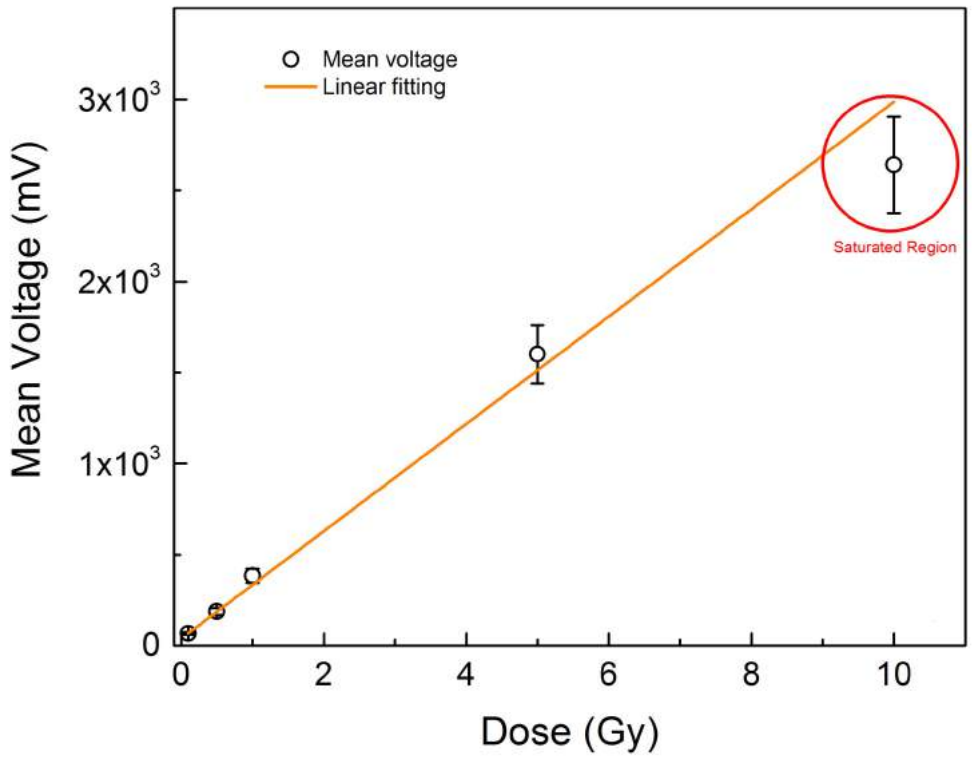


Figure 78: Linear behavior between dose and light emission using LYNX SiPM.

The comparison of the responses of the different samples, visible in Figure 79, shows that the reader is able to measure different amounts of photoluminescence emission light.

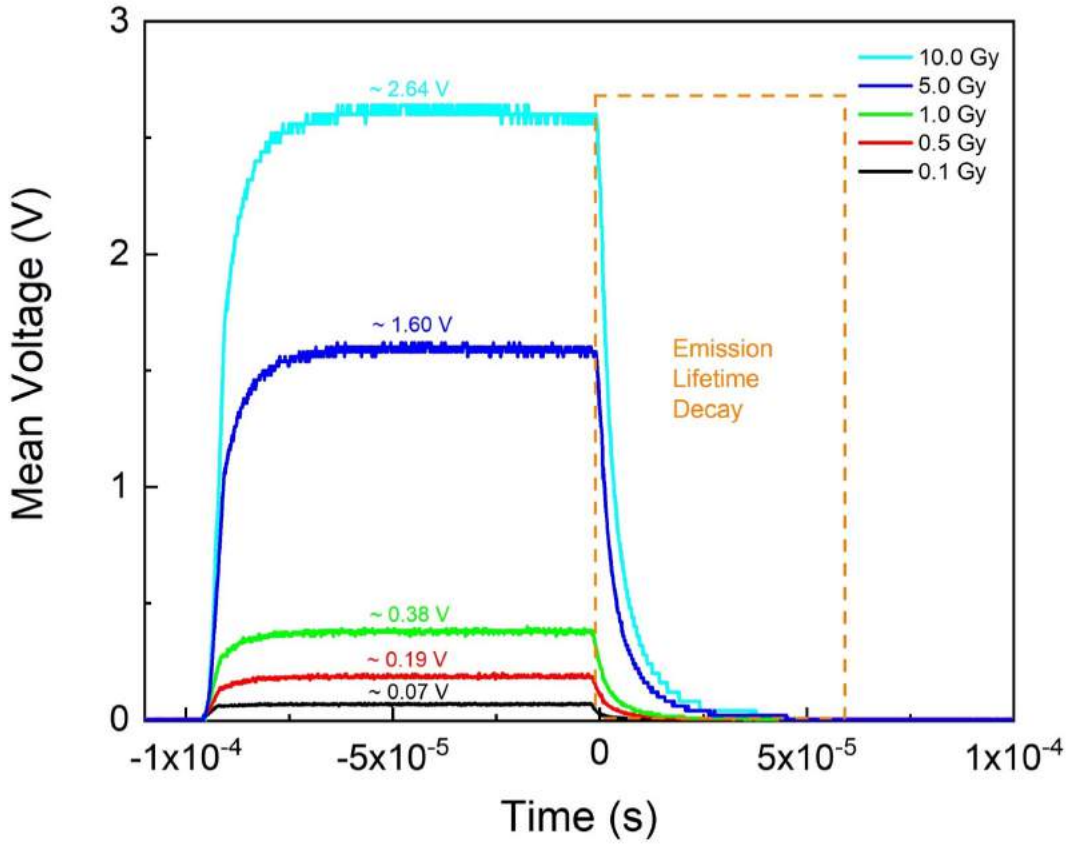

Figure 79: Comparison graphs of all the irradiated samples using the 100 μs stimulation pulse.

The study of the lifetime decay emission from the samples is another type of measurement that can be done with this new photoluminescence reader. As shown in the previous graph (Figure 79) the emission lifetime decay is acquired by the system in the period during which the LED is off.

To avoid the SiPM saturation with the highest-dose sample the intensity of the LED stimulation light was decreased, and the time duration of the pulse was also decreased from 100 μs to 10 μs using the fast LED driver to better evaluate the emission lifetime decay.

In the following graph (Figure 80), the same type of measurements is shown however using the new LED driver to generate a stimulation pulse of 10 μs instead of 100 μs.

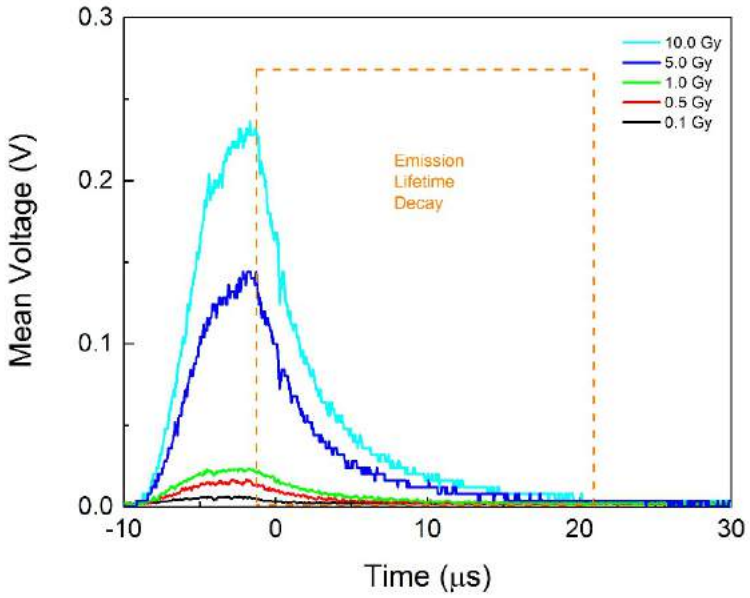


Figure 80: Comparison graphs of all the irradiated samples using the 10 μs stimulation pulse.

All lifetime decays of each photoluminescence signal presented in Figure 80 were analyzed by taking into account only the fall time of the signal, i.e., by examining just the region depicted by the dashed orange rectangle from the respective figure. An example of this procedure is shown in Figure 81, while Figure 82 shows the exponential decay fitting from the signal fall time.

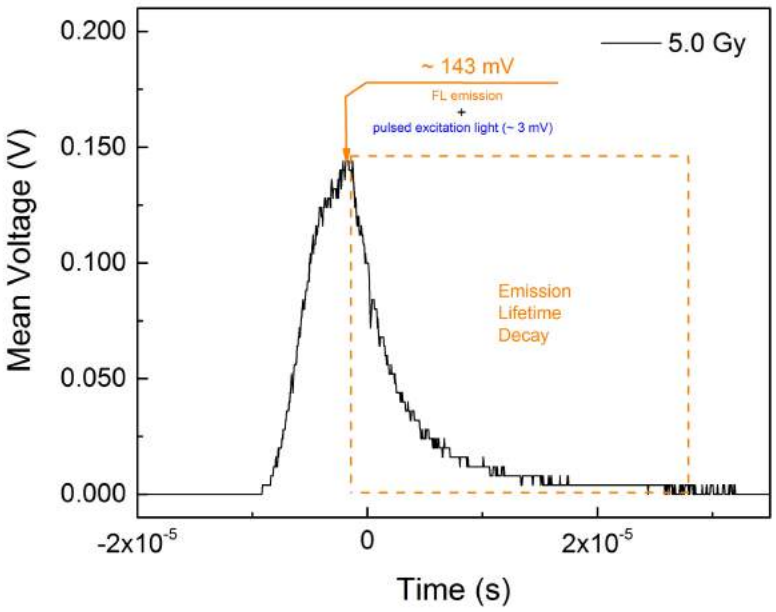


Figure 81: Output signal for the 5 Gy sample using the 10 μs stimulation pulse.

The lifetime decay values obtained by Ihara, Yohei, et al [96] are between 3.8 and 4.3 μs, which is in perfect accordance with the value obtained for our RPLGD sample irradiated with 5 Gy dose.

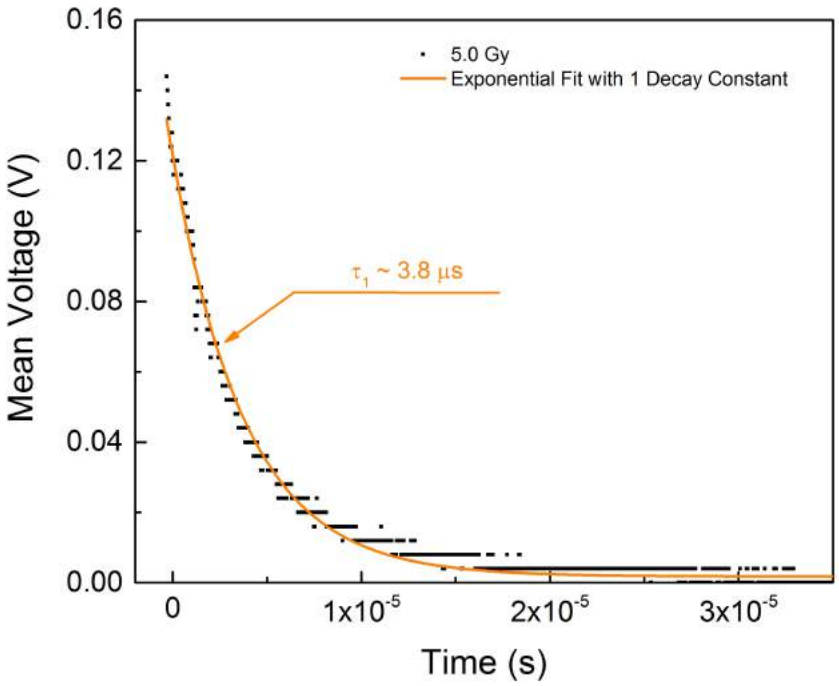


Figure 82: Emission lifetime decay fitting for the 5 Gy sample (10 μs)

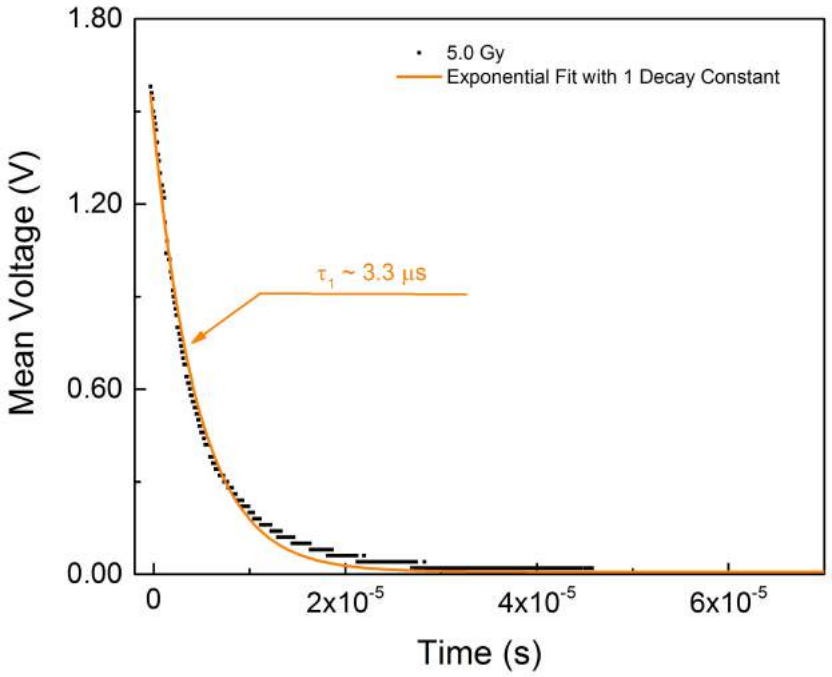


Figure 83: Emission lifetime decay fitting for the 5 Gy sample (100 μs)

Further research and probably more improvements on the optical setup presented are necessary to study the lifetime decay thoroughly. Also, this optoelectronic apparatus responds only to signals within the microseconds, limiting the analysis of faster photoluminescence phenomena, i.e., in the order of nanoseconds. Although, the lifetime decay constants obtained for the regimes between 10 μs (Figure 82) and 100 μs (Figure 83), were almost the same, showing that for the response time is not an issue.

The Figure 71 and Figure 84 clearly shows that in this work, was achieved the highest reproducibility of the results in terms of RPL signal versus dose, for the range between 0.1 Gy to 10 Gy. Once that we were able to achieve the same linear behavior (R=0.994 and R=0.998) with two different optical systems, in which the common denominator was the SiPM and the collection of the emission light at 90 degrees. Further investigations will show if this linear trend will continue with doses above 30 Gy, once that the 30 Gy sample was already tested in the second apparatus and the linear trend was maintained (Figure 84).

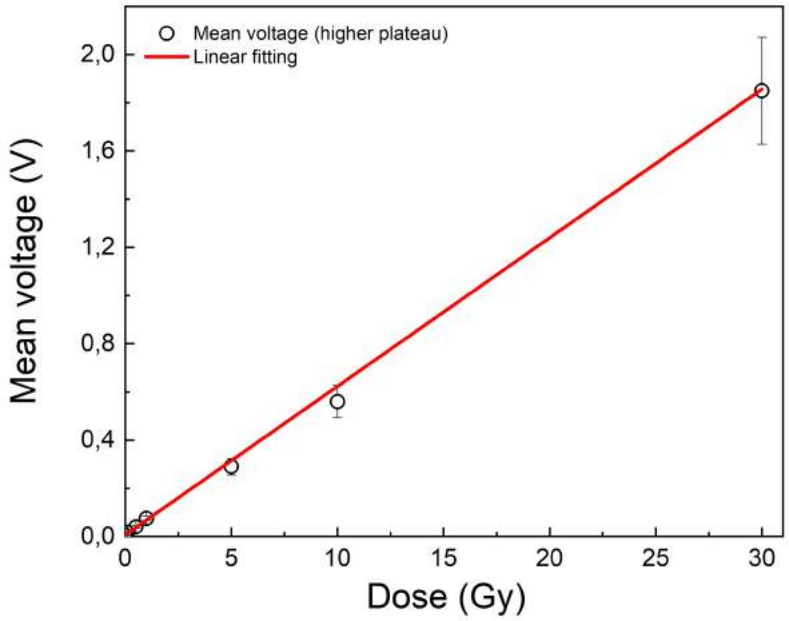


Figure 84: Linear behavior between dose and light emission using the new LED driver.

# 6 Conclusions and future perspectives

In this thesis, the applications of SiPMs in different research fields, like biological and radiological photonics, was evaluated. The numerous appealing features of SiPMs are the reason for their wide acceptance and success [97]. These photodetectors are compact and very powerful, capable of detecting low light intensities, even a single photon. They are highly customizable because the number of their micro-cells can be chosen depending on the specific application, e.g., in relation to the active area to be examined. Great opportunities are offered by their ability to detect light at low optical intensities with an efficiency comparable to PMTs, combined with the insensitivity to magnetic fields typical of semiconductors: this feature has led to an entirely new field of medical imaging with "hybrid" systems such as PET-MRI scanners.

In this work, a beta detection probe was realized, show how SiPM coupled with plastic scintillator is a good solution for scintillation detector, so for development an intravascular beta probe. Exciting developments are at the horizon such as the possibility of realizing endovascular and intra-myocardial SiPM based probes for an integrated theranostic system utilizing molecularly-targeted radiotracers to achieve localized intra-myocardial therapeutic delivery [36].

An experimental set-up was developed and studied for the realization of an ultra-compact and low-cost reader for luminescent dosimeters. Our completely modular configuration, based on LED as stimulation and SIPM as detector, allows the study the properties of many luminescent materials, such as OSL dosimeters: by varying the elements of the modules, it is possible to obtain many configurations optimized for the reading different dosimetric materials.
To obtain different stimulation or reading wavelengths it is sufficient to change the couplings between the LEDs and SiPM and the optical filters. An ongoing research project offered the opportunity to test the system with Radio-Photo-Luminescence Glass Dosimeters (RPLGD) that are stimulated with UV wavelength and emit around 550 nm.

The possibility of creating an ultra-compact reader is an optimal solution especially in the field of dating, where to carry out on-site analysis guarantees optimization of resources, avoiding further campaigns to collect samples in case of errors, and for luminescence-

based dating in harsh environments [98-101]. A portable luminescence reader based on PMTs has already been described [102], but it is not ideal for in field use due to PMT mechanical fragilities.

Being composed of all elements available on the market, the reader is characterized by a low cost that will allow access to a larger number of research centers. Moreover, it will guarantee a future technological development that will follow the new and improved technologies in the field of photonic detection: new detectors or LEDs can in fact be installed in the module with small changes in the support structure.

The optical system proposed in this work is very versatile, thanks to the modular solution and to SiPMs flexibility is possible to build reader for a large variety of materials. In addition, the small size, the affordable cost and the mechanical robustness will allow to design and build a portable optical system for environmental campaign. So, the field of radiation detection with optically stimulated luminescent materials will greatly benefit from the SiPM's ruggedness.

## References


1. Perumal, V. and U. Hashim, *Advances in biosensors: Principle, architecture and applications.* Journal of Applied Biomedicine, 2014. **12**(1): p. 1-15.

2. Newell, A., *Nonlinear optics*. 2018: CRC Press.

3. Abegão, L.M., et al., *Second-and third-order nonlinear optical properties of unsubstituted and mono-substituted chalcones.* Chemical Physics Letters, 2016. **648**: p. 91-96.

4. Santos, F.A., et al., *Bromo-and chloro-derivatives of dibenzylideneacetone: Experimental and theoretical study of the first molecular hyperpolarizability and two-photon absorption.* Journal of Photochemistry and Photobiology A: Chemistry, 2018.

5. Kamada, K., et al., *Boron Difluoride Curcuminoid Fluorophores with Enhanced Two-Photon Excited Fluorescence Emission and Versatile Living-Cell Imaging Properties.* Chemistry–A European Journal, 2016. **22**(15): p. 5219-5232.

6. Abegão, L.M., et al., *Oxazole Dyes with Potential for Photoluminescence Bioprobes: A Two-Photon Absorption Study.* The Journal of Physical Chemistry C, 2018. **122**(19): p. 10526-10534.

7. Bui, A.T., et al., *Cationic two-photon lanthanide bioprobes able to accumulate in live cells.* Inorganic chemistry, 2016. **55**(14): p. 7020-7025.

8. Miao, F., et al., *Novel fluorescent probes for highly selective two-photon imaging of mitochondria in living cells.* Biosensors and Bioelectronics, 2014. **55**: p. 423-429.

9. Baugh, L.M., et al., *Non-destructive two-photon excited fluorescence imaging identifies early nodules in calcific aortic-valve disease.* Nature biomedical engineering, 2017. **1**(11): p. 914.

10. Knoll, G.F., *Radiation detection and measurement*. 2010: John Wiley & Sons.

11. Valença, J., et al., *Optically stimulated luminescence of borate glasses containing magnesia, quicklime, lithium and potassium carbonates.* Radiation Physics and Chemistry, 2017. **140**: p. 83-86.

12. Souza, S., et al., *OSL films for in-vivo entrance dose measurements.* Radiation Measurements, 2017. **106**: p. 644-649.

13. d'Errico, F. and A. Di Fulvio, *Advanced readout methods for superheated emulsion detectors.* Review of Scientific Instruments, 2018. **89**(5): p. 053304.

14. d'Errico, F., et al., *Optical readout of superheated emulsions.* Radiation Measurements, 2008. **43**(2-6): p. 432-436.

15. Saveliev, V., *Silicon photomultiplier-new era of photon detection*, in *Advances in Optical and Photonic Devices*. 2010, InTech.

16. Dautet, H., et al., *Photon counting techniques with silicon avalanche photodiodes.* Applied optics, 1993. **32**(21): p. 3894-3900.

17. Golovin, V. and V. Saveliev, *Novel type of avalanche photodetector with Geiger mode operation.* Nuclear Instruments and Methods in Physics Research Section A: Accelerators, Spectrometers, Detectors and Associated Equipment, 2004. **518**(1-2): p. 560-564.

18. Somov, S.V., I. Tolstukhin, and A.S. Somov, *Application of the silicon photomultipliers for detectors in the GlueX experiment.* Physics Procedia, 2015. **74**: p. 74-80.

19. Barbosa, F., et al., *Silicon photomultiplier characterization for the GlueX barrel calorimeter.* Nuclear Instruments and Methods in Physics Research Section A: Accelerators, Spectrometers, Detectors and Associated Equipment, 2012. **695**: p. 100-104.

20. Kovaltchouk, V., et al., *Comparison of a silicon photomultiplier to a traditional vacuum photomultiplier.* Nuclear Instruments and Methods in Physics Research Section A: Accelerators, Spectrometers, Detectors and Associated Equipment, 2005. **538**(1-3): p. 408-415.

21. Sciuto, E.L., et al., *Photo-physical characterization of fluorophore Ru(bpy) 3 2+ for optical biosensing applications.* Sensing and Bio-Sensing Research, 2015. **6**: p. 67-71.

22. Shin, Y.-H., et al., *A hand-held fluorescent sensor platform for selectively estimating green algae and cyanobacteria biomass.* Sensors and Actuators B: Chemical, 2018. **262**: p. 938-946.

23. Grigoriev, E., et al., *Silicon photomultipliers and their bio-medical applications.* Nuclear Instruments and Methods in Physics Research Section A: Accelerators, Spectrometers, Detectors and Associated Equipment, 2007. **571**(1-2): p. 130-133.

24. Stortz, G., et al., *Performance of a PET Insert for High-Resolution Small-Animal PET/MRI at 7 Tesla.* J Nucl Med, 2018. **59**(3): p. 536-542.

25. Stoykov, A., et al., *A SiPM-based ZnS:6LiF scintillation neutron detector.* Nuclear Instruments and Methods in Physics Research Section A: Accelerators, Spectrometers, Detectors and Associated Equipment, 2015. **787**: p. 361-366.

26. Kim, J.H., H.M. Park, and K.S. Joo, *Development of compact and real-time radiation detector based on SiPM for gamma-ray spectroscopy.* Journal of Instrumentation, 2018. **13**(07): p. P07018-P07018.

27. Ferocino, E., et al., *High throughput detection chain for time domain optical mammography.* Biomedical optics express, 2018. **9**(2): p. 755-770.

28. Farina, A., et al., *Time-Domain Functional Diffuse Optical Tomography System Based on Fiber-Free Silicon Photomultipliers.* Applied Sciences, 2017. **7**(12): p. 1235.

29. Santangelo, M.F., et al., *Integrating printed microfluidics with silicon photomultipliers for miniaturised and highly sensitive ATP bioluminescence detection.* Biosens Bioelectron, 2018. **99**: p. 464-470.

30. Santangelo, M.F., et al., *Si Photomultipliers for Bio-Sensing Applications.* IEEE Journal of Selected Topics in Quantum Electronics, 2016. **22**(3): p. 335-341.

31. Schaart, D.R., et al., *Advances in digital SiPMs and their application in biomedical imaging.* Nuclear Instruments and Methods in Physics Research Section A: Accelerators, Spectrometers, Detectors and Associated Equipment, 2016. **809**: p. 31-52.

32. Mazzillo, M., et al., *Silicon photomultiplier technology at STMicroelectronics.* IEEE Transactions on Nuclear Science, 2009. **56**(4): p. 2434-2442.

33. Bocci, V., et al. *The ArduSiPM a compact trasportable software/hardware data acquisition system for SiPM detector*. in *Nuclear Science Symposium and Medical Imaging Conference (NSS/MIC), 2014 IEEE*. 2014. IEEE.

34. Hudin, N., et al., *Characterization and Optimization of silicon photomultipliers for the development of intraoperative beta probes.* Nuclear Instruments and Methods in Physics Research Section A: Accelerators, Spectrometers, Detectors and Associated Equipment, 2012. **695**: p. 242-246.

35. Conti, M., *Focus on time-of-flight PET: the benefits of improved time resolution.* European journal of nuclear medicine and molecular imaging, 2011. **38**(6): p. 1147-1157.

36. Stendahl, J., et al., *Development and Testing of an Integrated Catheter for Beta Detection and Intramyocardial Therapeutic Delivery.* Journal of Nuclear Medicine, 2016. **57**(supplement 2): p. 1949-1949.

37. Staglianò M., C.A., Souza S.O., d'Errico F., *Dosimetria OSL con un lettore versatile e miniaturizzato a SiPM.* Atti del Convegno Nazionale AIRP di Radioprotezione, Salerno, Italy,, 2017: p. pag. 68-76.

38. Yukihara, E., et al., *Application of the optically stimulated luminescence (OSL) technique in space dosimetry.* Radiation Measurements, 2006. **41**(9-10): p. 1126-1135.

39. Yukihara, E., S.J.P.i.M. McKeever, and Biology, *Optically stimulated luminescence (OSL) dosimetry in medicine.* Physics in Medicine & Biology, 2008. **53**(20): p. R351.

40. Aitken, M.J., *Introduction to optical dating: the dating of Quaternary sediments by the use of photon-stimulated luminescence*. 1998: Clarendon Press.

41. Rhodes, E., *Optically stimulated luminescence dating of sediments over the past 200,000 years.* Annual Review of Earth Planetary Sciences, 2011. **39**: p. 461-488.

42. Jacobs, Z., and Richard G. Roberts, *Advances in optically stimulated luminescence dating of individual grains of quartz from archeological deposits.* Evolutionary Anthropology: Issues, News, and Reviews, 2007. **16.6**: p. 210-223.

43. Yukihara, E.G. and S.W. McKeever, *Optically stimulated luminescence: fundamentals and applications*. 2011: John Wiley & Sons.

44. Bortolot, *A new modular high capacity OSL reader system.* Radiation Measurements, 2000. **32**(5-6): p. 751-757.

45. Kearfott, K.J. and W.G. West, *An affordable optically stimulated luminescent dosimeter reader utilizing multiple excitation wavelengths.* Applied Radiation and Isotopes, 2015. **104**: p. 87-99.

46. Smetana, F., et al., *A portable multi-purpose OSL reader for UV dosimetry at workplaces.* Radiation Measurements, 2008. **43**(2-6): p. 516-519.

47. Eckert, P., et al., *Characterisation studies of silicon photomultipliers.* Nuclear Instruments and Methods in Physics Research Section A: Accelerators, Spectrometers, Detectors and Associated Equipment, 2010. **620**(2-3): p. 217-226.

48. Piatek, S.S., *Physics and Operation of an MPPC.* Hamamatsu Corporation and New Jersey Institute of Technology, 2014.

49. Barbarino, G., et al., *Silicon photo multipliers detectors operating in geiger regime: an unlimited device for future applications*, in *Photodiodes-World Activities in 2011*. 2011, InTech.

50. Buzhan, P., et al., *Silicon photomultiplier and its possible applications.* Nuclear Instruments and Methods in Physics Research Section A: Accelerators, Spectrometers, Detectors and Associated Equipment, 2003. **504**(1-3): p. 48-52.

51. Dolgoshein, B., et al., *Status report on silicon photomultiplier development and its applications.* Nuclear Instruments and Methods in Physics Research Section A: Accelerators, Spectrometers, Detectors and Associated Equipment, 2006. **563**(2): p. 368-376.

52. Hawkes, R., et al. *Silicon photomultiplier performance tests in magnetic resonance pulsed fields*. in *Nuclear Science Symposium Conference Record, 2007. NSS'07. IEEE*. 2007. IEEE.

53. Frach, T., et al. *The digital silicon photomultiplier—Principle of operation and intrinsic detector performance*. in *Nuclear Science Symposium Conference Record (NSS/MIC), 2009 IEEE*. 2009. IEEE.

54. Garutti, E. and Y. Musienko, *Radiation damage of SiPMs.* arXiv preprint arXiv:1809.06361, 2018.

55. Diblen, F., et al., *Radiation hardness of dsipm sensors in a proton therapy radiation environment.* IEEE Transactions on Nuclear Science, 2017. **64**(7): p. 1891-1896.

56. Bohn, P., et al., *Radiation damage studies of silicon photomultipliers.* Nuclear Instruments and Methods in Physics Research Section A: Accelerators, Spectrometers, Detectors and Associated Equipment, 2009. **598**(3): p. 722-736.

57. Garutti, E., et al., *Silicon Photomultiplier characterization and radiation damage investigation for high energy particle physics applications.* Journal of Instrumentation, 2014. **9**(03): p. C03021.

58. Luka, G., et al., *Microfluidics Integrated Biosensors: A Leading Technology towards Lab-on-a-Chip and Sensing Applications.* Sensors (Basel), 2015. **15**(12): p. 30011-31.

59. Fernández Gavela, A., et al., *Last advances in silicon-based optical biosensors.* Sensors, 2016. **16**(3): p. 285.

60. Chien, P.J., et al., *Optical isopropanol biosensor using NADH-dependent secondary alcohol dehydrogenase (S-ADH).* Talanta, 2016. **159**: p. 418-424.

61. Vasilantonakis, N., et al., *Refractive index sensing with hyperbolic metamaterials: strategies for biosensing and nonlinearity enhancement.* Opt Express, 2015. **23**(11): p. 14329-43.

62. Wu, X., et al., *Dye-Sensitized Core/Active Shell Upconversion Nanoparticles for Optogenetics and Bioimaging Applications.* ACS Nano, 2016. **10**(1): p. 1060-6.

63. Vasquez, E.S., et al., *Bioluminescent magnetic nanoparticles as potential imaging agents for mammalian spermatozoa.* J Nanobiotechnology, 2016. **14**: p. 20.

64. Santangelo, M., et al. *CY5 fluorescence measured with silicon photomultipliers*. in *Biomedical Circuits and Systems Conference (BioCAS), 2014 IEEE*. 2014. IEEE.

65. Dey, D. and T. Goswami, *Optical biosensors: a revolution towards quantum nanoscale electronics device fabrication.* J Biomed Biotechnol, 2011. **2011**: p. 348218.

66. Jiang, S., et al., *Ultra-low noise and exceptional uniformity of SensL C-series SiPM sensors*, in *Optical Components and Materials XII*. 2015.

67. Renna, L., et al., *Extremely integrated device for high sensitive quantitative biosensing.* Sensors and Actuators B: Chemical, 2015. **209**: p. 1011-1014.

68. Petralia, S., et al., *Sulfide Species Optical Monitoring by a Miniaturized Silicon Photomultiplier.* Sensors (Basel), 2018. **18**(3).

69. Nikl, M. and A. Yoshikawa, *Recent R&D trends in inorganic single-crystal scintillator materials for radiation detection.* Advanced Optical Materials, 2015. **3**(4): p. 463-481.

70. Buzhan, P., et al., *Large area silicon photomultipliers: Performance and applications.* Nuclear Instruments and Methods in Physics Research Section A: Accelerators, Spectrometers, Detectors and Associated Equipment, 2006. **567**(1): p. 78-82.

71. Kuper, K., et al., *On reachable energy resolution of SiPM based scintillation counters for X-ray detection.* Journal of Instrumentation, 2017. **12**(01): p. P01001.

72. Grodzicka-Kobylka, M., et al., *Study of n-γ discrimination by zero-crossing method with SiPM based scintillation detectors.* Nuclear Instruments and Methods in Physics Research Section A: Accelerators, Spectrometers, Detectors and Associated Equipment, 2018. **883**: p. 159-165.

73. Pavlov, N., G. Mashlum, and D. Meier. *Gamma spectroscopy using a silicon photomultiplier and a scintillator*. in *Nuclear Science Symposium Conference Record, 2005 IEEE*. 2005. IEEE.

74. Grodzicka-Kobylka, M., et al., *Silicon photomultipliers in scintillation detectors used for gamma ray energies up to 6.1 MeV.* Nuclear Instruments and Methods in Physics Research Section A: Accelerators, Spectrometers, Detectors and Associated Equipment, 2017. **874**: p. 137-148.

75. Park, J.H., et al. *Analysis of changes in environmental radiation, and three types of environmental radiation detector performance comparisons*. in *Advancements in Nuclear Instrumentation Measurement Methods and their Applications (ANIMMA), 2013 3rd International Conference on*. 2013. IEEE.

76. Nodari, B., et al. *Radon fast detection and environmental monitoring with a portable wireless system*. in *Advances in Sensors and Interfaces (IWASI), 2015 6th IEEE International Workshop on*. 2015. IEEE.

77. Buzhan, P., A. Karakash, and Y. Teverovskiy, *Silicon Photomultiplier and CsI (Tl) scintillator in application to portable H*(10) dosimeter.* Nuclear Instruments and Methods in Physics Research Section A: Accelerators, Spectrometers, Detectors and Associated Equipment, 2017.

78. Foster, M. and D. Ramsden. *A compact neutron detector based on the use of a SiPM detector*. in *Nuclear Science Symposium Conference Record, 2008. NSS'08. IEEE*. 2008. IEEE.

79. Osovizky, A., et al., *Design of an ultrathin cold neutron detector.* Nuclear Instruments and Methods in Physics Research Section A: Accelerators, Spectrometers, Detectors and Associated Equipment, 2018. **893**: p. 1-9.

80. Osovizky, A., et al., *SENTIRAD—An innovative personal radiation detector based on a scintillation detector and a silicon photomultiplier.* Nuclear Instruments and Methods in Physics Research Section A: Accelerators, Spectrometers, Detectors and Associated Equipment, 2011. **652**(1): p. 41-44.

81. Moutinho, L., et al., *Development of a scintillating optical fiber dosimeter with silicon photomultipliers.* Nuclear Instruments and Methods in Physics Research Section A: Accelerators, Spectrometers, Detectors and Associated Equipment, 2014. **735**: p. 640-643.

82. Garcia-Parra, R., et al., *Performance of beta-and high-energy gamma probes for the detection of cancer tissue in experimental surgical resection beds.* Annals of nuclear medicine, 2011. **25**(7): p. 486-493.

83. Dolinsky, S., G. Fu, and A. Ivan, *Timing resolution performance comparison of different SiPM devices.* Nuclear Instruments and Methods in Physics Research Section

A: Accelerators, Spectrometers, Detectors and Associated Equipment, 2015. **801**: p. 11-20.

84. Hutton, B.F., K. Erlandsson, and K. Thielemans, *Advances in clinical molecular imaging instrumentation.* Clinical and Translational Imaging, 2018. **6**(1): p. 31-45.

85. Del Guerra, A., et al., *Silicon Photomultipliers (SiPM) as novel photodetectors for PET.* Nuclear Instruments and Methods in Physics Research Section A: Accelerators, Spectrometers, Detectors and Associated Equipment, 2011. **648**: p. S232-S235.

86. Omidvari, N., et al., *MR-compatibility assessment of MADPET4: a study of interferences between an SiPM-based PET insert and a 7 T MRI system.* Physics in Medicine & Biology, 2018. **63**(9): p. 095002.

87. Bruschini, C., et al., *A Sensor Network Architecture for digital SiPM Based PET Systems.* IEEE Transactions on Radiation and Plasma Medical Sciences, 2018.

88. Carminati, M., et al., *SPECT/MRI INSERT Compatibility: Assessment, Solutions and Design Guidelines.* IEEE Transactions on Radiation and Plasma Medical Sciences, 2018.

89. Seifert, S., et al., *First characterization of a digital SiPM based time-of-flight PET detector with 1 mm spatial resolution.* Physics in Medicine & Biology, 2013. **58**(9): p. 3061.

90. Kwon, S.I. and J.S. Lee, *Signal encoding method for a time-of-flight PET detector using a silicon photomultiplier array.* Nuclear Instruments and Methods in Physics Research Section A: Accelerators, Spectrometers, Detectors and Associated Equipment, 2014. **761**: p. 39-45.

91. Katz, L., and A. So Penfold, *Range-energy relations for electrons and the determination of beta-ray end-point energies by absorption.* Reviews of Modern Physics, 1952. **24.1**.

92. McKeever, S. and M. Moscovitch, *On the advantages and disadvantages of optically stimulated luminescence dosimetry and thermoluminescence dosimetry.* Radiation protection dosimetry, 2003. **104**(3): p. 263-270.

93. Hsu, S.-M., et al., *Development and physical characteristics of a novel compound radiophotoluminescent glass dosimeter.* Radiation Measurements, 2008. **43**(2-6): p. 538-541.

94. Richter, D., A. Richter, and K.J.G. Dornich, *Lexsyg smart—a luminescence detection system for dosimetry, material research and dating application.* Geochronometria, 2015. **42**(1).

95. Huang, D.Y. and S.-M. Hsu, *Radio-photoluminescence glass dosimeter (RPLGD)*, in *Advances in Cancer Therapy*. 2011, InTech.

96. Ihara, Y., et al., *A compact system for measurement of radiophotoluminescence of phosphate glass dosimeter.* Radiation Measurements, 2008. **43**(2-6): p. 542-545.

97. Staglianò M., A.L., Chierici A. and d'Errico F, *Silicon photomultiplier current and prospective applications in biological and radiological photonics.* International Journal of Science & Engineering, 2018. **4(10)**: p. 10-29.

98. Li, S.-H., et al., *OSL dating of sediments from deserts in northern China.* Quaternary Geochronology, 2007. **2**(1-4): p. 23-28.

99. Arnold, L.J. and R.G. Roberts, *Stochastic modelling of multi-grain equivalent dose (De) distributions: Implications for OSL dating of sediment mixtures.* Quaternary Geochronology, 2009. **4**(3): p. 204-230.

100. Lewis, C.J., et al., *Climatic implications of correlated Upper Pleistocene glacial and fluvial deposits on the Cinca and Gállego Rivers (NE Spain) based on OSL dating and soil stratigraphy.* Global and Planetary Change, 2009. **67**(3-4): p. 141-152.

101. Lomax, J., A. Hilgers, and U. Radtke, *Palaeoenvironmental change recorded in the palaeodunefields of the western Murray Basin, South Australia–new data from single grain OSL-dating.* Quaternary Science Reviews, 2011. **30**(5-6): p. 723-736.

102. Stone, A., M. Bateman, and D. Thomas. *Dating large linear dunes in the southern Namib using OSL: single aliquot regeneration protocol and portable reader measurements*. in *EGU General Assembly Conference Abstracts*. 2014.